Implementation of Energy-Efficient System for Solar-Powered Pleasure Yacht using dc Architecture

K. Pit, ir. S. Qazi*, dr. ir. P Venugopal**, dr. ir. J.T.W. Berendsen***
*Daily Supervisor, **Assistant Professor, ***External Committee member
BSc. Thesis Electrical Engineering
University of Twente, Department of Electrical Engineering, Mathematics and Computer Science
August 8, 2022

***Abstract*—This thesis describes the design and simulation of a dc architecture-based system for an all-electric pleasure yacht. As the earth's natural resources start to deplete and the emission of greenhouse gasses needs to be drastically reduced, electrical substitutes for the old-fashioned fuel-powered maritime vessels start to become the new norm. A lot of research is executed in the field of hybrid-based propulsion systems, but very little for full E-systems. With the EV industry being a booming market, the maritime sector is lagging behind. From this point of view, an energy-efficient solar-powered pleasure yacht is designed and simulated using a PV array as the main source of electric energy. Efficient converters are designed for the allowance of both uni- and bidirectional power flow powering the (variable) auxiliary load and ensuring a steady dc bus voltage. A 15-kW asynchronous motor employing v/f control is used for the propulsion and the dynamic behaviour of the system is verified through simulations using MATLAB/Simulink. Moreover, the applicability of various solid-state devices is inspected to maximize the efficiency of the onboard system. Finally, a cost analysis spanning 24h operation is included and compared with the conventionally-used propulsion system.**

***Index Terms*—Electric Ships, E-mobility, Soft-switching, Solar boats**

I. Introduction

The demand for clean, carbon-neutral and renewable energy-based electric power-trains is rising and is likely to follow this uptrend in the coming decades. Maritime transport is one of the biggest drivers of the European economy. However, it is also a large and growing source of greenhouse gas emissions. In 2018, the global shipping industry was responsible for the emission of 1076 million tonnes of CO_2, equalling about 2.9% of the global human activity emission. Futurewise, regarding the emission levels, they are projected to increase from 90% to 130% of 2008 emissions by 2050 taking into consideration a wide range of plausible scenarios. If the impact of shipping activities on the climate sets follows its projected growth rate, it would not be in accordance with the objectives of the Paris Agreement [1]. So, the maritime sector, as one of the most important worldwide industries, is lagging behind in this field often still making use of old diesel engines. Of the exhaust gasses emitted by these engines, Nitrogen and Sulphur oxides are the most severe ones. These gases have adverse effects on the environment resulting in a strengthened greenhouse effect and global warming with all its consequences.

This is the reason for many countries to invest in projects replacing the old-fashioned fossil fuel-based Maritime Vessels (MVs) with their electrically powered substitute. This thesis proposes an energy-efficient dc-based system architecture for application in small pleasure yachts, as for the current situation this is the most plausible field of application.

Electric maritime vessels (EMVs) use the same principle as used in other EVs; storing energy onboard by using a number of batteries as their main source of power and electric drives for propulsion. The electric drive typically features an inverter, electric motor, and a form of closed loop control [2]. In addition, a photovoltaic (PV) array can be added to generate even more power by converting energy radiated out by the sun to stored electrical energy.

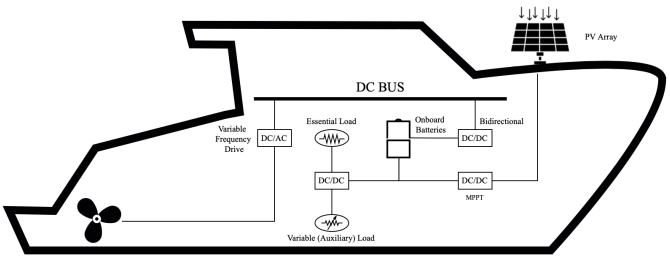

Fig. 1. Onboard electric energy system including several power conversion stages.

Figure 1 shows a block diagram of the to-be-implemented electric propulsion system. This system is to be placed in the hull of the vessel, consisting of an electric motor, multiple power converting stages (both dc-to-dc and dc-to-ac), a PV array, a battery pack, a fixed load and variable auxiliary load and the battery pack including a Battery Management System (BMS) [2].

Section II imposes a basic solution to the system given in Fig. 1. For the electric propulsion system, a 3-phase induction motor is chosen, implementing volts per hertz control. A PWM inverter functions as the speed drive wherein PI control is used to execute closed-loop operation. Furthermore, both boost- and buck-based converters are needed to power a variety of loads. To power the motor from the dc bus a DAB converter is introduced allowing bidirectional power flow. Here Single Phase Shift Modulation (SPSM) is applied to control the power flow with a discrete PID controller. Thirdly, an MPPT

system with Perturb and Observe-based algorithm is used to charge the batteries again using PWM together with a Battery Management System (BMS) and discrete PI control. All stages are verified by simulations using MATLAB/Simulink.
Section III builds on the previous section by introducing ZVS/ZCS and implementing a full bridge series resonant converter (FBSRC). A resonant tank is mathematically derived and designed in a discrete PI control loop. An analysis is included on the preferred application regions for MOSFETs vs IGBTs and different insulator materials are discussed that may impact the energy efficiency of the system.
Section IV discusses the expected power consumption on the basis of load curves for an arbitrary trip over a 24-hour time span.

II. Operating System

A. Asynchronous Motor

To get from point A to point B by means of electric propulsion, an electric motor is needed. For this a 3-Φ asynchronous induction motor is chosen due to its high power performance requirement, greater durability suppressing maintenance costs and its broad control and configuration requirements [3]. The asynchronous motor specifications can be found in section VII-A. They are chosen on behalf of the desired application, which is a reasonably sized (10-15m) pleasure yacht as this is the interesting market for complete electric propulsion. The synchronous speed is given by [4]:

$$N_s = \frac{120 * f}{P} \tag{1}$$

The induced EMF in the induction motor is given by [4]:

$$E_s = 4.44 k_{\omega s} \phi f N \tag{2}$$

Where $k_{\omega s}$ is a winding factor, ϕ is the resultant flux, f the supply frequency and N TF turn ratio. From (2), it can be seen that in case the supply frequency is changed, the induced stator EMF will change accordingly maintaining the same flux. If the stator voltage drop is ignored, the motor terminal voltage (V_s) is proportional to the induced EMF. To minimize losses every motor is flux rated, so V_s is controlled by the supply frequency keeping the ratio V_s/f constant (also referred to as volt per hertz control) [4].

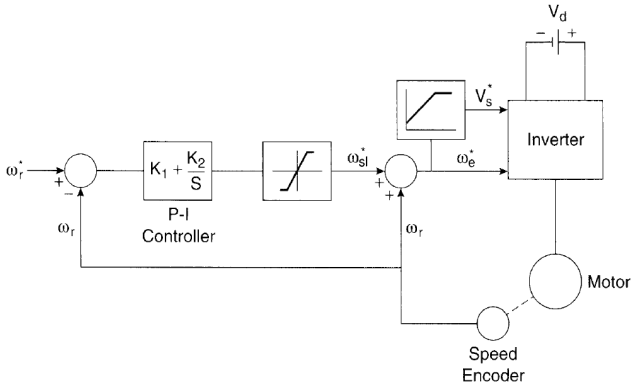

Fig. 2. Closed loop speed control with volts/Hz control and slip regulation [5].

In order to actively control rotor speed and drive the inverter, the above-mentioned strategy was applied (see Fig. 2). Sinusoidal Pulse Width Modulation (sPWM) is used to drive the power transistors for the 3-Φ inverter (each 120° out of phase), which effectively regulates the current flow. The output voltage controls the on time (t_{on}) and the frequency controls the timing of the switches [6]. The triangular carrier wave function was implemented with a switching frequency of 25 kHz.
The dc bus voltage is calculated using the sPWM modulation index (m) and the AC RMS line voltage relation [6]:

$$\frac{\sqrt{3} m V_D}{2\sqrt{2}} = V_{l\_RMS} \tag{3}$$

In order to avoid overmodulation (m $>$ 1) m is set to 0.95 together with the AC RMS line voltage rated at 400V, now [6]:

$$V_D = \frac{2\sqrt{2} V_{l\_RMS}}{\sqrt{3} m} = 687.58V \tag{4}$$

To be able to accurately control the rotor speed, closed-loop control is introduced. For this, a discrete PI controller was designed as it offers robust control in a wide range of operating conditions and for its functional simplicity.
PI(D) control uses three separate gain factors each having its own influence on the control. The proportional gain (P) influences the response time, but if chosen too high the system starts oscillating. The integral (I) gain takes care of a (possible) offset in steady state. The differential (D) gain is usually kept low as it makes the system strongly sensitive to noise. On top of that, it ensures a more strong reaction to changes in the error term.
A discrete PI feedback control is designed, with gains $K_p = 1.00035$ and $K_i = 0.1$. To even further increase the accuracy of the model, there is compensation for the slip speed, which is the difference between the synchronous speed (see 1) and the rotor operating speed. As the speed loop error generates the slip command (ω_{sl}) together with the designed PI controller (limiter is left out as this affects certain speed in- and decreases). This slip is added to the feedback rotor speed. Now as the reference speed increases, the machine is able to accelerate freely and as the reference speed decreases the drive

switches to a 'dynamic braking mode' where it decelerates with a factor of $-\omega_{sl}$. [5]
Implementing this in MATLAB Simulink, the following control network was used:

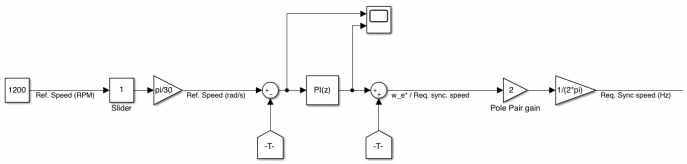

Fig. 3. MATLAB closed loop implementation of volt per hertz control of a variable frequency drive using PI control.

For a full system overview, see Sec. VII-A. As can be seen from Fig. 3, an additional gain of two was added in the control loop to compensate for the difference between electrical and mechanical speed, which is dependent on the number of machine poles (P) according to [7]:

$$\omega_e = \frac{P}{2}\omega_m \tag{5}$$

Furthermore, the load torque (T_m) is variable with the rotational speed (N) squared according to [8]:

$$T_m = G_r k_q \rho D^5 N^2 \tag{6}$$

In which G_r is the gearbox ratio, k_q the torque coefficient, ρ the water density and the propellor diameter. the corresponding values are 1/5, 0.06, 1026 kg/m^3 and 0.30 m respectively [8]. Simulation results can be seen in Fig. 4, showing that it successfully responds to changes in reference speed with reasonable overshoot and settling time.

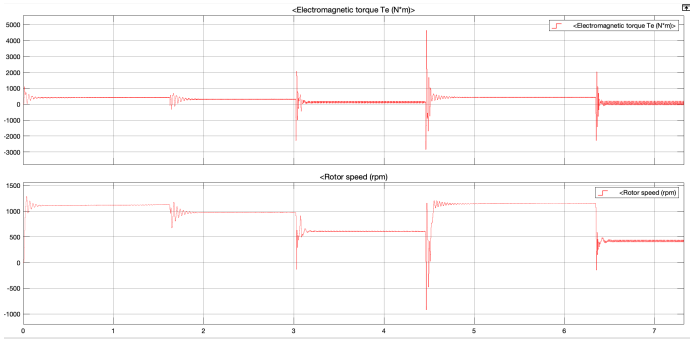

Fig. 4. Simulink results displaying electromagnetic torque (Nm) and rotor speed (RPM) over time.

The load torque should not exceed the maximum allowable torque (Nm) at any given motor power (W) and rotational rotor speed (rad/s). Using:

$$T = \frac{P}{N} \tag{7}$$

When looking at Fig. 4, at 600 RPM (= 62.83 rad/s) and for the given motor power, this results in:

$$T = \frac{15 * 10^3}{62.83} = 239\ Nm \tag{8}$$

Again referring back to figure 4, one is able to see that at a rotational speed of 600 RPM the torque stabilizes at 114 Nm. Regarding efficiency, it is measured by dividing input over output power for a wide range of reference speeds (400/800/1200 RPM):

$$\eta_{m,avg} = \frac{\frac{4.750*10^4}{5.581*10^4} + \frac{1.715*10^4}{1.829*10^4} + \frac{4.265*10^3}{5.268*10^3}}{3} * 100\% = 86.6\% \tag{9}$$

B. Battery

To power the system, a source is needed that can provide enough energy storage, such that a reasonable range and auxiliary power demand can be achieved. Extensive research has been done for dc-based systems in recent years, which shows increasing efficiency due to simple-to-implement control methods and less conducting material. dc-based systems are gaining popularity for smaller MVs. As for this category, mostly owned by private persons, reliable and fast protection circuits (BMS) are becoming affordable. Regarding the voltage ratings, it can range from 400 V in small vessels, as is used in modern EVs, up to tens of kilovolts in large vessels with power in the order of megawatts.
Batteries come in a variety of types. Cobalt Oxide batteries are the most common type of chemistry used in marine applications. Future-wise Lithium Titanate Oxide, Nickel Metal Hydride, and solid-state electrolyte-based batteries are good competitors. As the requirements regarding energy density are less strict for the maritime sector than for terrestrial EVs, future storage systems for ships are likely to differ. Taking reliability into consideration it takes higher precedence, as ships often operate in remote places not being able to charge and seek help immediately. This introduces the necessity of the presence of an emergency generator [8].
It is chosen to implement a 120V 100kWh Li-ion battery to take care of all power facilities onboard being in alignment with what is used in the EV industry nowadays.

C. Charging Battery

Implementing a photovoltaic (PV) array onboard will provide for a small amount of energy generation extending the range of the ship. There are numerous ways to do so but to efficiently charge the battery and be able to achieve the highest possible efficiency, a Maximum Power Point Tracking (MPPT) algorithm is required. The principle is based on keeping a good adaptation between the PV array and the connected load to ensure maximum power delivery. Fig. 5 shows the nonlinear relations of a PV cell, varying according to its two input parameters; environmental temperature and irradiation [9].

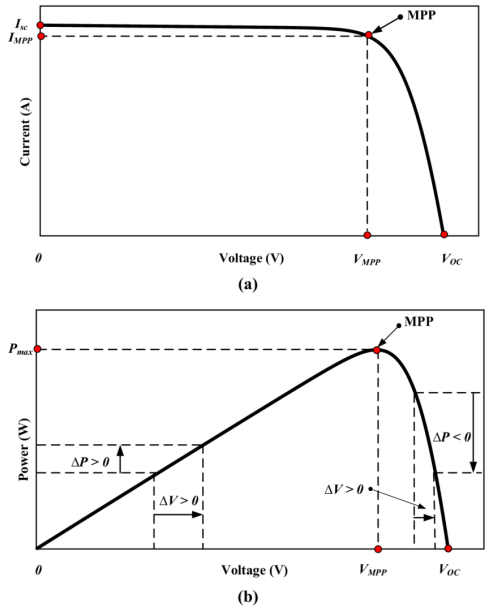

Fig. 5. PV characteristic curves for Perturb & Observe MPPT implementation [10].

1) Control Method: MPPT algorithms come in direct and indirect methods, with the direct method(s) being more accurate as they continuously respond to the optimal situation under influence of its above mentioned input parameters. The simplest direct MPPT implementation is the Perturb and Observe (P&O) algorithm, given in Fig. 5 based on [9].

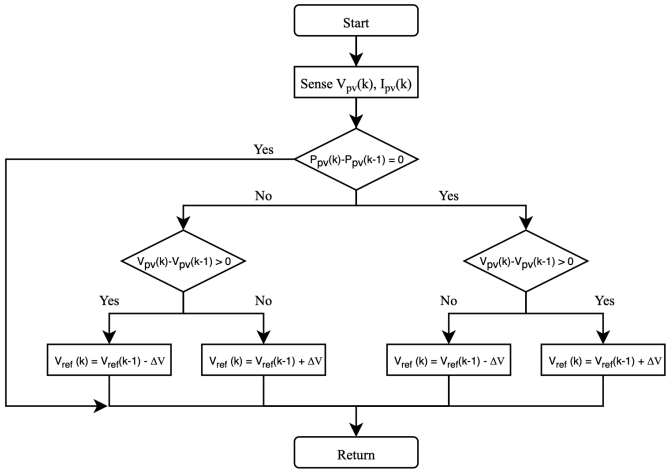

Fig. 6. Perturb and Observe algorithm principle.

As the name suggests, the algorithm is based on perturbation of the system by either de- or increasing V_{ref} effectively controlling the duty cycle of the semiconductor switching devices. It measures the PV output voltage and current (effectively measuring power) and compares the sample at time instant k to the power at the previous sample (k-1). In case both are equal, no action will be taken as the MPP is reached. If not, it checks whether the power at the current time sample is either higher or lower. Based on this it checks the voltages and either de- or increases it accordingly.
Implementing this algorithm in MATLAB Simulink, will result in the circuitry given in Fig. 7.

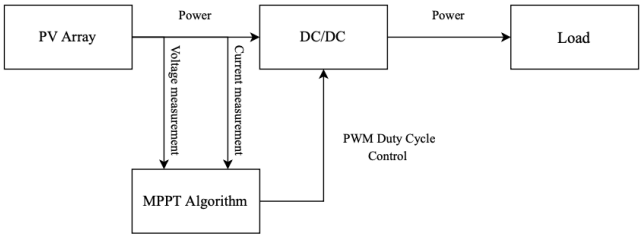

Fig. 7. Block diagram of MPPT control circuitry architecture using P&O algorithm.

It is chosen to use the Bosch Solar Energy c-SI M 60-225-16, due to its high quality, performance, reliability and its salt corrosion resistance [11]. The full list of panel parameters can be found in Sec. VII-C. The PV array comprises 3 parallel strings of one PV panel, each capable of delivering 225 Wp leading to a total capacity of 0.675 kWp under environmental conditions of $25°C$ and irradiance of 1 kW/m2 (see Fig. 10). The simulations are executed using a single panel.
As the battery voltage is chosen at 120V, a step up converter is needed. For accurate control closed loop MPPT is used implementing a discrete PI controller and Pulse Width Modulation (PWM) with a switching frequency of 25 kHz.

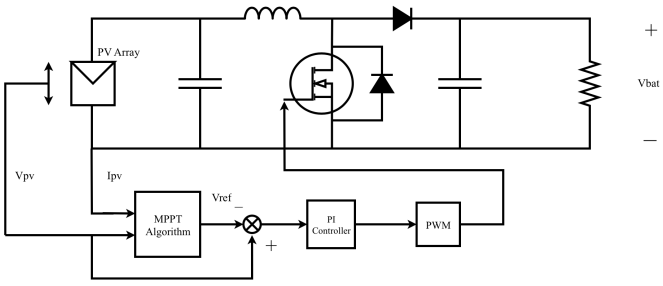

Fig. 8. P&O algorithm based MPPT closed loop control with boost converter.

Fig. 8 shows the implemented circuitry. The capacitor present at the input is there to reduce the ripple voltage amplitude, set to 1000 μF. The working principle of the boost converter is based upon the energy storage in the inductor. As the switch is closed the current increases as the circuit is almost short-circuited. The magnetic field in the inductor increases, storing electrical energy in the inductor. As the switch opens, the current decreases and the induced magnetic field collapses. The stored energy is released, reversing the inductor potential. Now the PV array, seen as a voltage source, is in series with the inductor, it boosts up the voltage see Fig. 9. The function of the diode is to ensure that the output capacitor cannot discharge via the inductor in case its potential exceeds V_{pv}.

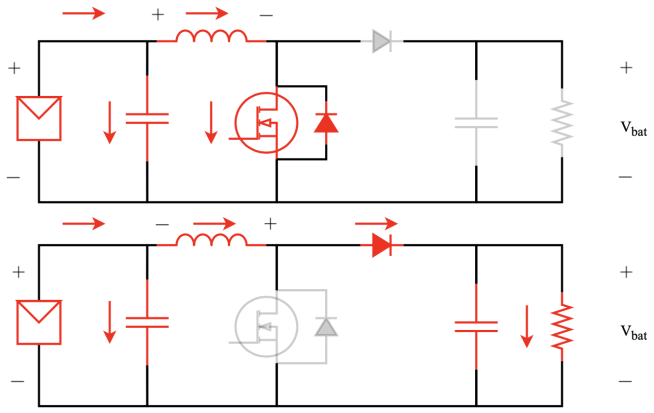

Fig. 9. Boost converter working principle with switch closed (top) and open (bottom) and current paths in red.

For the output voltage, the following relation holds:

$$V_o = L * \frac{dI}{dt} \tag{10}$$

Either increasing the inductor (L) or the switching frequency (dI/dt) result in a higher output voltage. The allowed current ripple (ΔI) is set at 5% and for the voltage ripple (ΔV) 1% is chosen. The input current is given as:

$$I_{in} = \frac{P_{max}}{V_{in,min}} = \frac{225W}{20V} = 11.75A \tag{11}$$

The current ripple then equals $\Delta I = 0.05 * 11.75 = 0.59A$ and for the voltage ripple $\Delta V = 120 * 0.01 = 1.20V$. The output current is given as:

$$I_o = \frac{P_{max}}{V_o} = \frac{225W}{120V} = 1.875A \tag{12}$$

Having this and using a switching frequency of 25 kHz, values for the inductance and capacitance can be derived [12]:

$$L = \frac{V_{in} * (V_o - V_{in})}{f_s * \Delta I * V_o} = 1.13mH \tag{13}$$

$$C = \frac{I_o * (V_o - V_{in})}{f_s * \Delta V * V_o} = 52\mu F \tag{14}$$

The implemented circuitry in MATLAB Simulink is given in Fig. VII-D. The chosen panel has specific I-V and P-V characteristics for different levels of irradiation (see Fig. 10).

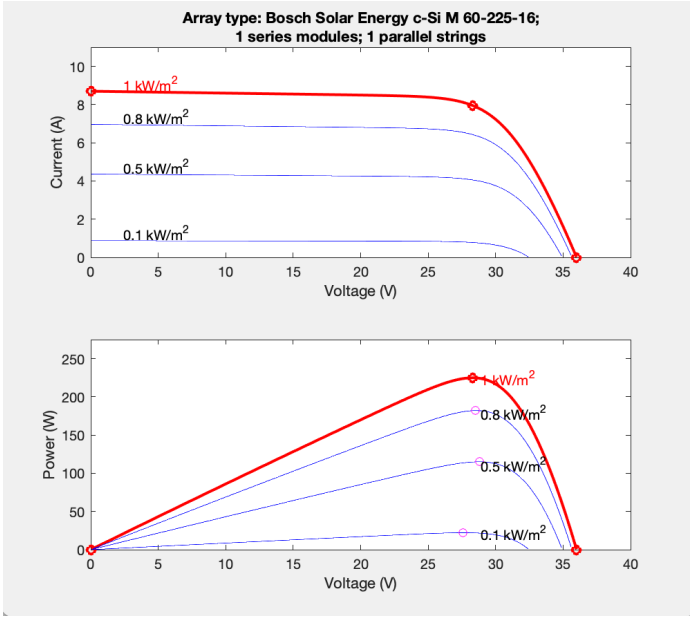

Fig. 10. I-V and P-V characteristics of the Bosch Solar Energy c-SI M 60-225-16 for different levels of irradiation.

Now using these levels of irradiation and plotting the panel output (voltage, current and power) and to maintain MPPT a discrete PI controller is designed, with gains $K_p = 1$ and $K_i = 1$, and with that a saturation limit of $0 < L < 1$ is imposed.

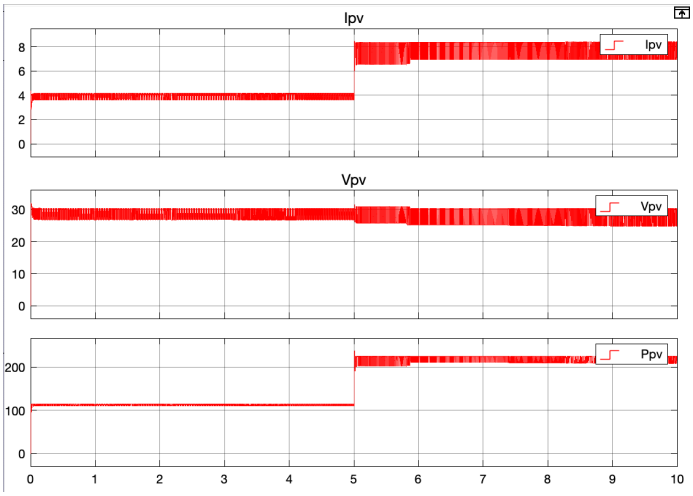

Fig. 11. Panel voltage (V_{pv}), current (I_{pv}) and power (P_{pv}) plotted for different levels of irradiation W/m^2.

Fig. 11 shows that both for an irradiation of 500 W/m^2 and 1000 W/m^2 the model is succesfully able to achieve MPPT. The average efficiency is measured over a wide reference range of irradiance (100/500/1000 W/m^2) by dividing the mean output over input power:

$$\eta_{pv,avg} = \frac{\frac{18.3}{22.1} + \frac{107.5}{113.7} + \frac{206.1}{218.8}}{3} * 100\% = 90.5\% \tag{15}$$

2) Battery Management System: As the chosen battery is of a Li-ion type, it needs protection to prevent it from blow-up caused by over- or undercharging. To do so, in the MPPT algorithm a check-up is included, which does the following. It checks both battery voltage and SOC. The battery comprises 33 Li-ion cells which have a save voltage range between 2.7-4.2 volts [13]. This leads to a breakdown voltage of 33*2.7 = 89.1 V and overcharge at 33*4.2 = 138.6 V. When the battery exceeds a SOC of 100% or reaches the breakdown voltage limits it detaches the solar panel from the boost converter by means of a switch until discharging ensures it is within limits again.

D. Variable (Auxiliary) Load

Not only the propulsion system needs power, a marine vessel can have several types of (variable) loads such as pumps, fans, refrigeration units, communication technology such as radar, lights etc. Depending upon the type, size and state of operation of the ship any of these can be in use and have a power demand from the onboard system [8]. As the battery voltage was set at 120V and most of the load functions at 12V dc, a step-down converter is needed. The working principle of this type of converter is rather similar to that of the previously explained boost converter shown in Fig.12.

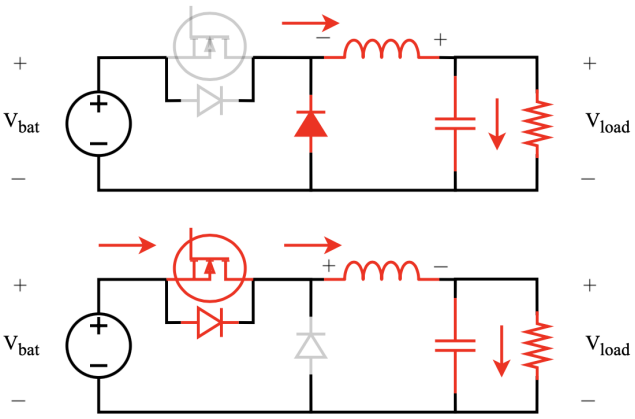

Fig. 12. Buck converter working principle with switch open (top) and closed (bottom) and current paths in red.

As the inductor charges and discharges by changing polarity as the switch closes and opens, the voltage is stepped down as the inductor absorbs charge.
The required duty cycle needed for the MOSFET present at the gate is:

$$D = \frac{V_{out}}{V_{in}} = \frac{12}{120} = 0.1 \tag{16}$$

For the allowed voltage and current ripple (1% of V_o and 5% of I_{sc}) the following relations hold:

$$\Delta I = 0.05 * 362.17 = 18.11A \tag{17}$$

$$\Delta V = 0.01 * 12 = 0.12V \tag{18}$$

Using a switching frequency of again 25 kHz, then for the inductance (L) and capacitance (C) [14]:

$$L = \frac{V_o * (V_i - V_o)}{\Delta I * f_s * V_i} = \frac{12 * (120 - 12)}{18.11 * 25 * 10^3 * 120} = 23.85\mu H \tag{19}$$

$$C = \frac{\Delta I}{8 * f_s * \Delta V} = \frac{18.11}{8 * 25 * 10^3 * 0.12} = 754\mu F \tag{20}$$

A schematic on the circuitry implemented using a discrete PI controller, and PWM to control the switch gate is given in Fig. 12.

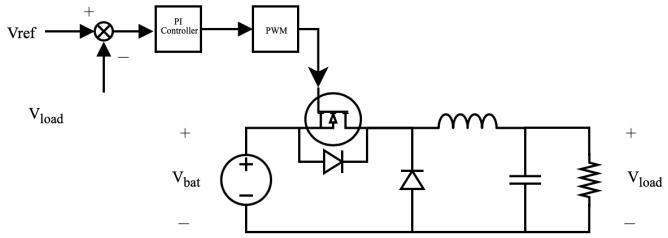

Fig. 13. System overview of closed loop control for buck converter using PI control and PWM.

A discrete PI controller is used in a negative feedback loop to actuate the output voltage, with gains $K_p = 1$ and $K_i = 1$. A saturation limit, $0 < L < 1$, is imposed to limit the controller output. Fig. 14 shows the simulation results implementing the above mentioned circuitry and using a 1Ω resistive load.

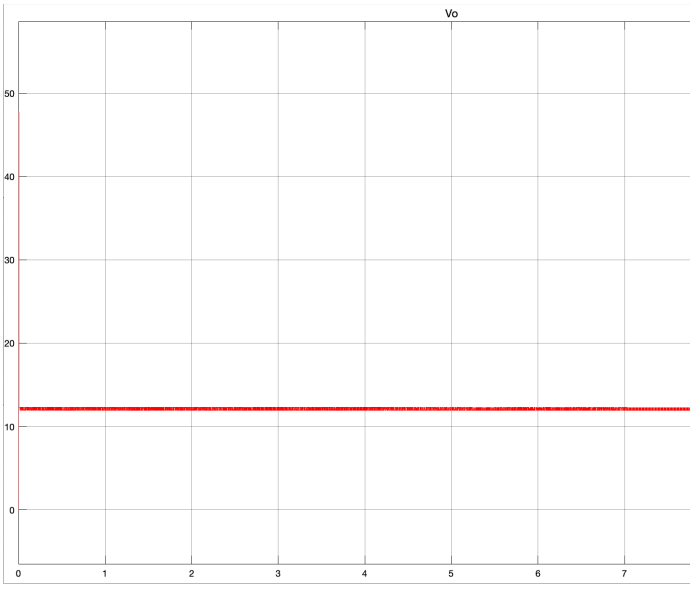

Fig. 14. Buck converter results using MATLAB Simulink plotting output voltage over a resistive load over time.

Fig. 14 shows that stepping down the voltage to 12V within a reasonable settling time is succesfully achieved. The average efficiency is measured over a wide load range according to the power demand given in Sec. VII-K (0.18/1.00/2.53 Ω) by dividing the mean output over input power:

$$\eta_{b,avg} = \frac{\frac{891}{1015} + \frac{158.2}{174.7} + \frac{59.8}{66.2}}{3} * 100\% = 89.6\% \tag{21}$$

E. Battery to dc Bus converter

To power the motor as efficient as possible a larger dc bus (>120V) is used based on the modulation index (m) and the line-line voltage of the induction motor, according to (4). To boost the battery voltage (LV) up to the required 690V and be able to handle such high power, three types of converters are suited:

- Push-Pull
- Half Bridge
- Full Bridge

The Dual Active Full bridge topology was chosen due to its best transformer core utilization, low device and component stresses and the ease of implementation of ZVS (Zero Voltage Switching) to further reduce switching losses and increase efficiency [15]. The basic DAB circuit implementation is given in Fig. 15.

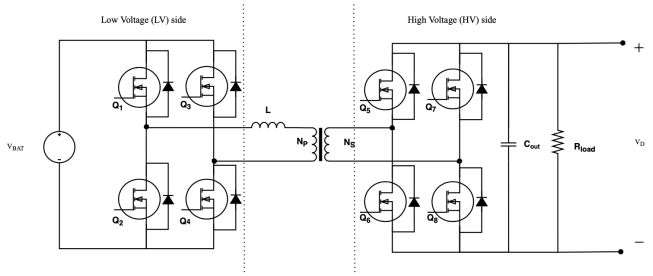

Fig. 15. Dual active bridge converter topology.

The principle of operation is as follows. It comprises two active full bridges interconnected through a transformer, with turn ratio n (N_p/N_s). The second bridge is phase shifted with respect to the LV full bridge to be able to control the power flow from the low- to the high-voltage side interfacing an RC load. In order to do so, time-varying voltages V_p and V_s need to be provided by both full bridges. Effectively converting a dc input signal to an intermediate ac signal. On the secondary TF side, it again converts this ac signal back to a high-voltage dc signal, lowering the current. This makes the analysis of the DAB much more simple, as the voltage sourced HV and LV side full bridges, can be replaced by voltage sources V1 and V2 (see Fig. 16) [16].

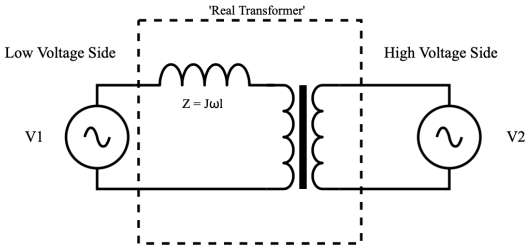

Fig. 16. Dual Active Bridge isolated dc/dc converter simplified equivalent circuit.

The inductance (L) is the internal leakage inductance of the transformer. As the TF is not perfectly coupled, each winding behaves as a self-inductance in series with its corresponding ohmic resistance. The switching devices are operated with switching frequency f_s and a duty cycle of 50% with the power flow, as explained previously, controlled by a phase shift Φ between the AC voltages present at both sides of the TF. This phase shift controls the amount of power transfer from the leading (LV) bridge to the lagging (HV) bridge according to [17]:

$$P = \frac{V1 * V2 * sin(\Phi)}{\omega * L} \tag{22}$$

The operation of the DAB is divided into four consecutive intervals. The voltage and current waveforms are depicted in Fig. 18. Fig. 17 based on [17] shows the circuit with corresponding current paths given in red.

1) Interval 1: During the first out of the four intervals the inductor current, i_L, is both negative and positive. Switches Q1 and Q4 on the primary (LV) bridge and switches Q6 and Q7 on the secondary (HV) side conduct. The voltage on the primary TF side is equal to $+V_{BAT}$ and on the primary side, the voltage is equal to $-V_D$. The slope of the current during this first interval is given by [17]:

$$\frac{di}{dt} = \frac{V_{BAT} + V_D}{L} \tag{23}$$

2) Interval 2: During the second interval, the current through the inductor is of positive nature only. As in the first interval, the voltage across the primary TF equals $+V_{BAT}$ and for the secondary side $+V_D$. The slope corresponding to the rising inductor current during this second interval is given by [17]:

$$\frac{di}{dt} = \frac{V_{BAT} - V_D}{L} \tag{24}$$

Switches 1 and 4 remain closed, but as the inductor current changes sign (becoming positive) the voltage on the secondary TF side is equal to $+V_D$. Switches Q5 and Q8 now close and start conducting. In between these intervals, there is a small interruption period in which all switches are open, called dead time [17].

3) Interval 3: During the third interval the inductor current is coming down with the same slope as it went for interval one, only with opposite sign [17]:

$$\frac{di}{dt} = -\frac{V_{BAT} + V_D}{L} \tag{25}$$

The voltage on the primary TF side equals $-V_{BAT}$ and for the secondary side $+V_D$. Q5 and Q8 remain closed, and since the voltage on the primary side switches sign Q2 and Q3 close and start conducting [17].

4) Interval 4: In the last interval the inductor current, i_L, remains negative. The primary side voltage equals $-V_{BAT}$ and for the secondary side $-V_D$. The voltage difference appears again across the inductor, equalling [17]:

$$\frac{di}{dt} = -\frac{V_{BAT} - V_D}{L} \tag{26}$$

Switches Q2 and Q3 remain closed as they did in the third interval. But, as the voltage on the secondary TF side switches from positive to negative it triggers Q6 and Q7 to close and start conducting [17].

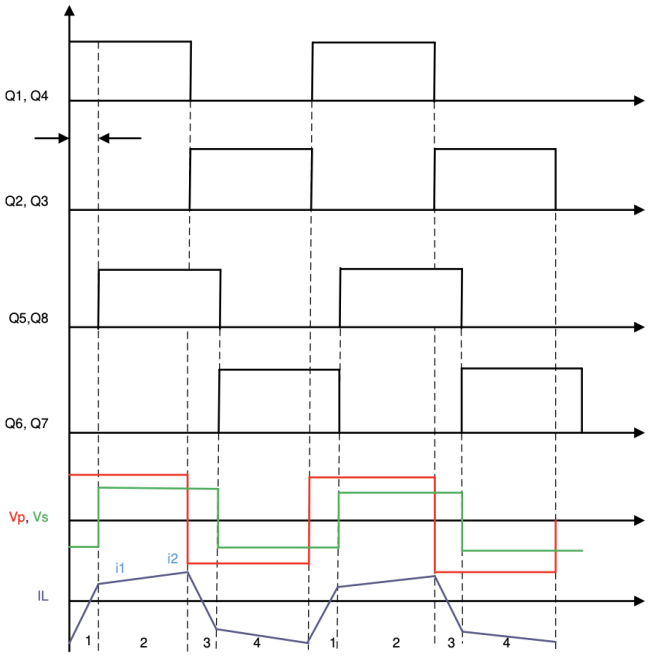

Fig. 18. Operating waveforms for Dual Active Bridge dc/dc converter [17].

When designing the DAB, one of the most decisive factors is the selection of the leakage inductance. The power transfer relation is given by [17]:

$$P = \frac{nV_{bat}V_D\Phi(\pi - \Phi)}{2\pi^2 f_s L} \tag{27}$$

Where n is the turn ratio, Φ is the phase shift between V_p and V_s, and f_s is the switching frequency. From (27) it becomes evident that for a low value of leakage inductance the highest power transfer can be realised for a fixed f_s and in- and output voltage. The maximum power transfer will occur at $\Phi = \frac{\pi}{2}$, therefore when later designing this DAB with closed loop form, the output saturation is limited as $0 < L < \frac{\pi}{2}$. In

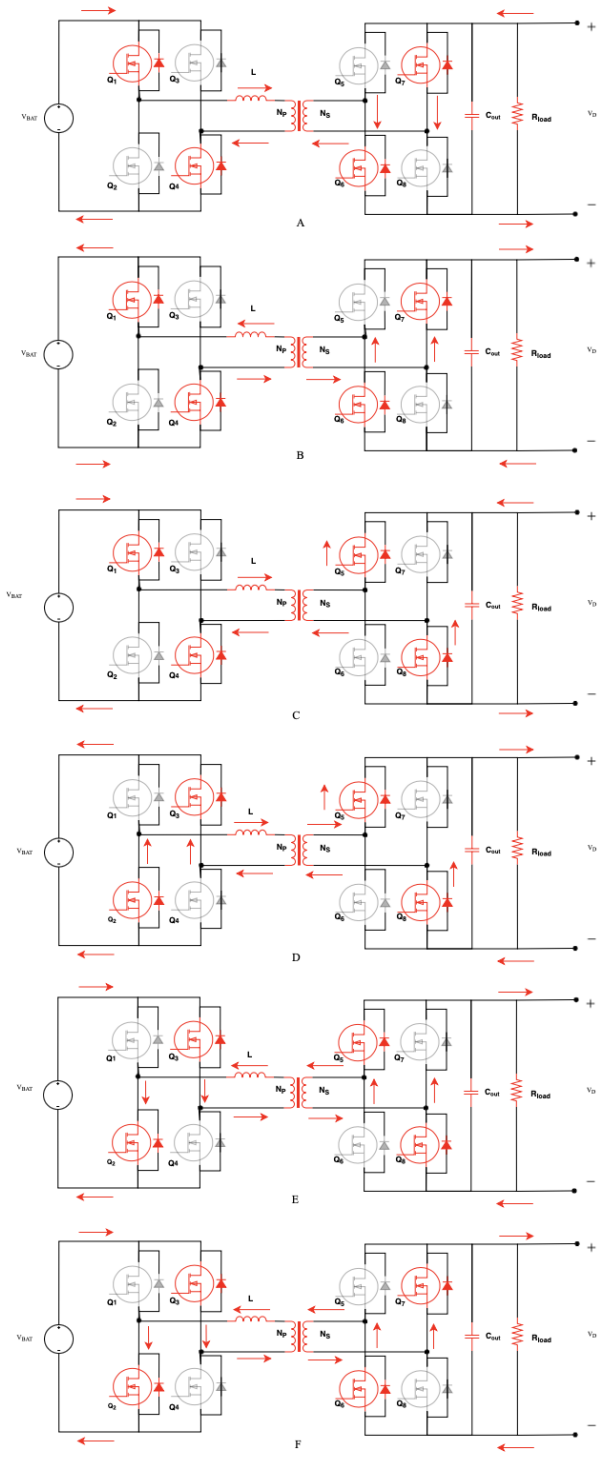

Fig. 17. Dual Active Bridge isolated dc/dc converter equivalent circuit including current paths for interval 1 with positive i_L (A) interval 1 with negative i_L (B) interval 2 (C) interval 3 with positive i_L (D) interval 3 with negative i_L (E) and interval 4 (F).

case the phase shift becomes negative the direction of power flow is reversed. Rewriting (27) results in an expression for the phase shift for a specific power transfer [17]:

$$\Phi = \frac{\pi}{2} * (1 - \sqrt{1 - \frac{8 f_s L P}{n V_{bat} V_D}}) \tag{28}$$

Where P denotes the output power, being equal to the nominal motor power (see Sec. VII-A).
The output capacitor should be chosen, such that it is able to handle the voltage ripple. It follows from [17]:

$$C \frac{dV_D}{dt} = \frac{V_{bat}}{X_L} \Phi (1 - \frac{\Phi}{\pi}) - \frac{V_D}{R_{load}} \tag{29}$$

So, for a given phase shift and inductance a specific capacitance is required keep the voltage ripple to a specified limit set by the design specifications. This effectively means that a higher capacitance value is required as the RMS capacitor current increases. The output capacitor (C_{out}) was chosen, such that it keeps the output voltage under a 1% ripple.
Again, to effectively control the DAB and ensure a stable output bus voltage it is made closed loop PI controlled as depicted in Fig. 19.

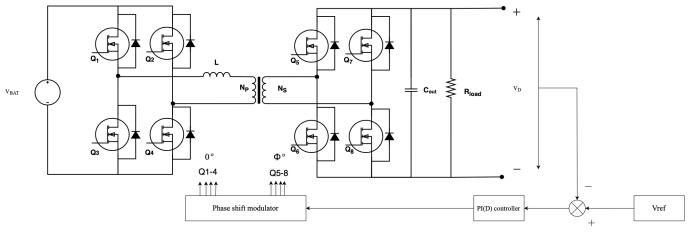

Fig. 19. Closed loop control of DAB using PI(D) control and single phase shift modulation.

It actuates the output dc bus voltage with gains $K_p = 0.05$, $K_i = 0.1$ and $K_d = 0.01$, with the derivative gain keeping the overshoot within reasonable numbers. The circuit was implemented in MATLAB Simulink accordingly using (22) and (27) - (29):

TABLE I
DAB COMPONENT PARAMETERS.

C_{out}	$1000\mu F$	Ripple Capacitance
L	$0.197\mu H$	Leakage Inductance
R_{load}	$> 31.74\Omega$	Load Impedance
n	0.12	TF turn ratio

To verify the correct operating of the DAB the output voltage and power are checked. The full MATLAB Simulink circuitry can be found in Sec. VII-E. Resistive loads may vary with the minimum value equalling:

$$R_{min} = \frac{V_d^2}{P} = \frac{690^2}{15 * 10^3} = 31.74\Omega \tag{30}$$

Fig. 20 and 21 show the output waveforms for both voltage and power.

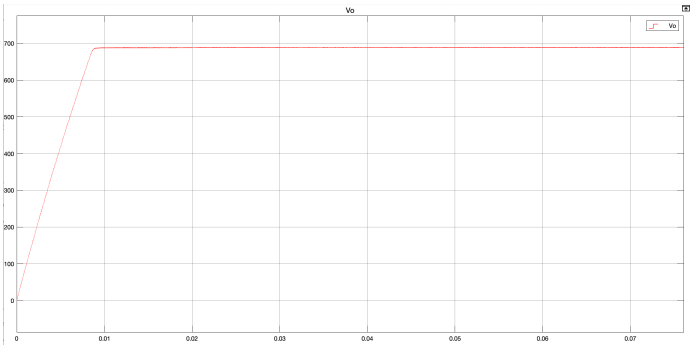

Fig. 20. Output voltage waveform of DAB dc/dc Converter.

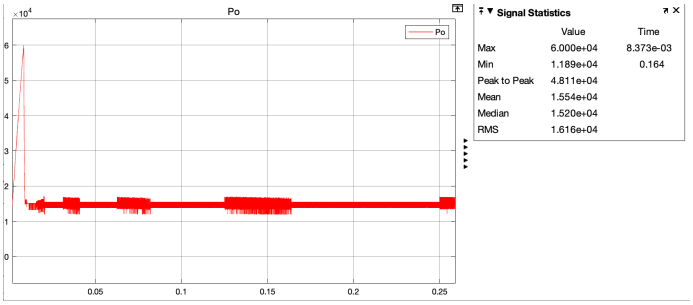

Fig. 21. Output Power waveform of DAB dc/dc Converter for 31.74Ω load resistance.

From these two figures it becomes clear that the output voltage and power correspond to the expected values meeting their design criteria. They settle within 10ms with satisfactory results regarding the voltage ripple of 6.9 Volts. The average efficiency is measured at 31.74-100 ohmic loads by dividing the mean output over input power:

$$\eta_{d,avg} = \frac{\frac{1.49*10^4}{1.56*10^4} + \frac{4.73*10^3}{5.40*10^3}}{2} * 100\% = 91.6\% \tag{31}$$

For high ohmic load, meaning low rotor speed, the magnetic field of the induction motor increases generating excessive heat and reduced efficiency is the result. Therefore, these ohmic loads exceeding 100Ω are not taken into account here.

F. System Integration

Now all the individual parts are completed they can be combined so that the system as a whole is operatable. For a full system overview, see Sec. VII-F.
First, the motor was attached to the DAB, leaving out the DAB resistive load. This gave errors regarding an unstable dc bus voltage and uncontrollable rotor speed. This is caused by the torque needed for the induction motor at start-up. In order for the load to be accelerated, the motor must generate a torque that exceeds the load requirement. The time the motor needs in order for the load to be accelerated up to the reference speed is dependent on the load inertia and the margin between the torque of the motor and the load curve also referred to as accelerating torque. As the starting current of an induction motor can be several higher than the full load current, high inrush currents magnetize the air gap between the stator and

rotor. The induced EMF in the rotor windings produces an electrical current, which in turn generates the motor torque. High inrush currents during start-up can result in large voltage dips for the dc bus voltage. A proposed solution is given in Sec. VI to overcome this problem.

A second and easier approach is redesigning the DAB. As the DAB was designed for nominal motor power of 15kW and torque being linearly proportional to power, see (7), it becomes evident that a re-design is needed due to the principle mentioned above. Using (27) either the turn ratio, n, or the inductance value, L, can be changed for the converter to allow for higher power ratings.

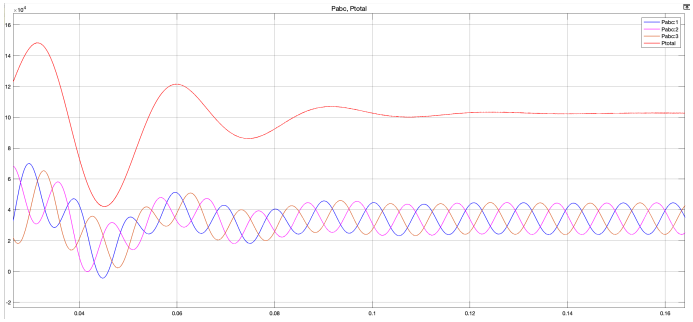

Fig. 22. Mean motor power during start-up for 3-Φ 15 kW induction motor.

Fig. 22 shows the mean power for all three phases directing the induction motor. It can be seen that during start-up values for the motor power can range up to $7 * 10^5$ VA due to high inrush currents. To be able to handle such powers the maximum output factor was scaled up with a factor of 5, effectively reducing the size of the leakage inductance with a factor of 5.

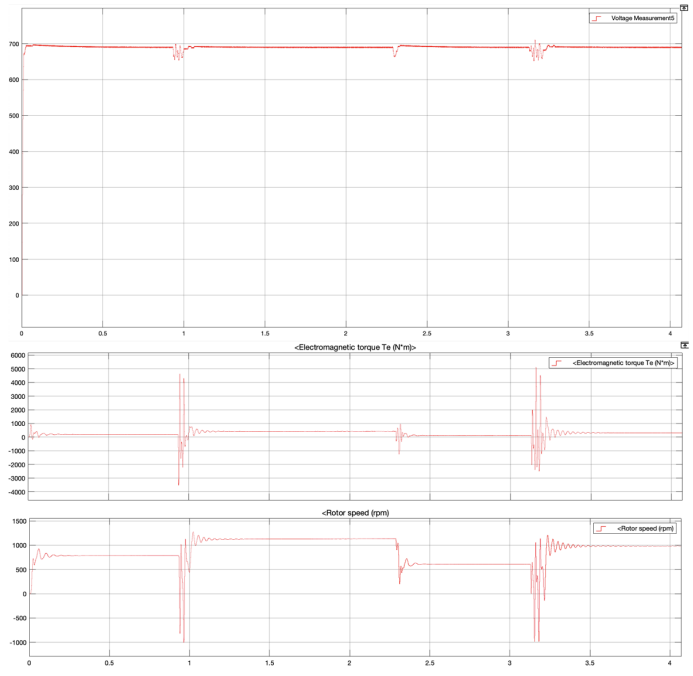

Fig. 23. Operating system dc bus voltage (top), electromagnetic motor torque (middle) and rotor speed (bottom).

Fig. 23 shows the dc bus voltage, Electromagnetic torque and rotor speed. Validating this with the results obtained stand-alone, given in figure 4, 20 and 21, it can be concluded that both the DAB and Volts per Hertz control of the induction motor still work satisfactorily.

Now the MPPT system and auxiliary load can be attached to complete the system. This succeeded without any complications due to robust control and no further load implications. For a full system overview see Sec. VII-F.

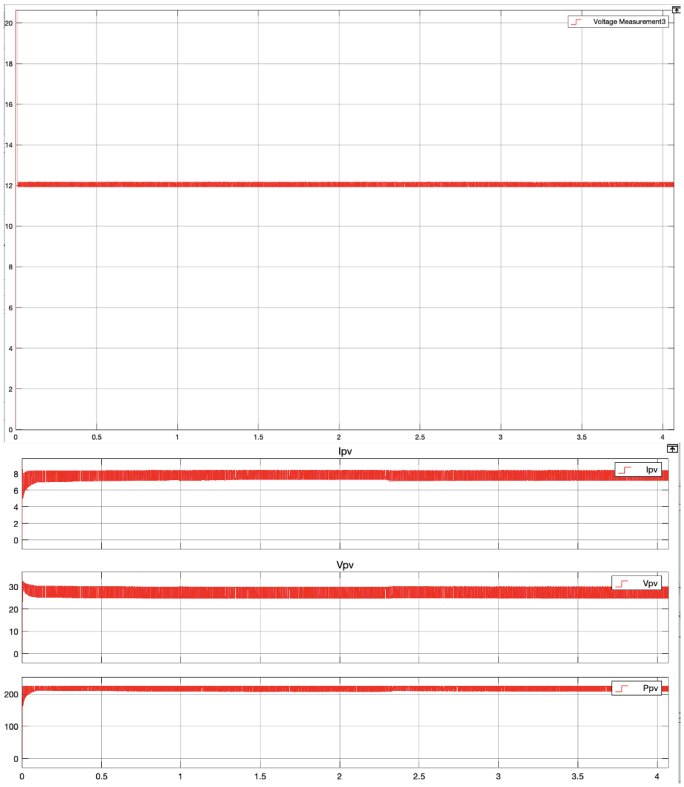

Fig. 24. Operating system buck converter voltage (top) and PV power (bottom).

G. MOSFET vs IGBT

Taking one step back, it is chosen to implement MOSFETs as transistor type. This choice is not directly evident and deserves substantiation. The MOSFET, being a semiconductor device, is able to act as both an insulator and conductor for consecutive time periods. For the voltage and switching frequency range, the system operates at, there are two types of transistors that remain applicable; the MOSFET and IGBT. For the preferred application regions regarding power and switching frequency see Fig. 25.

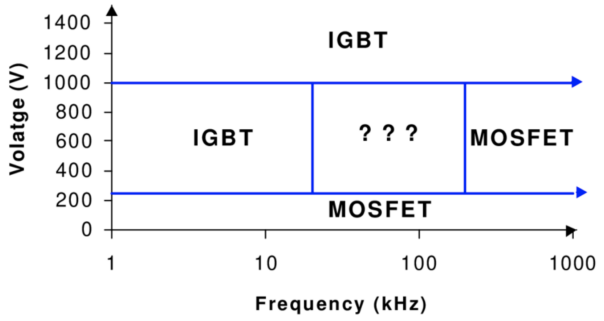

Fig. 25. Preferred area of application for MOSFETs and IGBTs [18].

From Fig. 25 it can be seen that for applications exceeding 1000V breakdown voltage the IGBT is the transistor of choice opposite to breakdown voltages below 250V where the MOSFET is preferred. In between, there is a shady area where either could be preferred based on the application taking cost, size, speed and thermal requirements into consideration [18].
The MOSFET is a 4-terminal device, driven by a gate signal present between gate (G) and source (S). The gate is made of metal separated from the source by a metal-oxide allowing for less power consumption. It has a positive temperature coefficient, meaning for increasing temperature internal resistances increase where the current density is at its highest reducing the effective current. This ensures less thermal runaway and a uniform current density. Generally speaking, MOSFETs have good high-frequency characteristics ranging from hundreds of kHz to several MHz. The downside happens in high voltage/current applications, where the internal FET's on-state resistance ensures significant power losses. Besides, MOSFETs are preferred in applications with wide line/load variations and long duty cycles [19] [20].
The IGBT is a 3-terminal device, driven by a control signal present between gate (G) and emitter (E). Its switch terminals are the collector and emitter. It uses the gate drive characteristics from the MOSFET and high current, low saturation voltage capabilities of the bipolar transistor. Therefore, it combines excellent performance in the lower frequency ranges ($<$20 kHz) and high power occasions. The on-state resistance, which was the limiting factor for high power application for the MOSFET, is small. Where the FET can be applied to wide line/load variations and large cycles the IGBT is at the other end preferably operating under narrow line/load variations and low duty cycles [19] [20].
Combining the system parameters with the advantages of both devices mentioned above it is chosen to implement MOSFETs. What switching frequency should then be chosen for the different subsystems. In general, it holds true that higher switching frequencies are better. So, it reduces physical component sizes and with that enlarges power density. The trade-off here is between reducing sizes and higher switching losses. And so these switching losses limit f_s.

H. Si vs SiC vs (GaN)

Converter efficiency is mainly determined by the performance of semiconductor devices. A MOSFET comprises three layers; a semiconductor layer, an insulator, and a metal layer being the gate. Different materials are being used, traditionally made of Silicon (Si) but as the demand for greater power density, better thermal performance and high-efficiency semiconductor devices grows Silicon Carbide (SiC) and Gallium Nitride (GaN) take the number one spot outperforming Si.
Differentiating between these types is based on a number of material parameters affecting the FETs performance [21]:

- Bandgap
- Saturation velocity
- Electron mobility
- Thermal conductivity
- Breakdown field

SiC and GaN transistors are wide bandgap (measured in eV) devices, meaning they require a relatively high energy level to move electrons from their valence band to the conduction band, in contrast to Silicon (Si, bandgap: 1.1 eV). This leads to higher critical breakdown voltages. The device is able to withstand higher voltages in the same package or the insulation can be reduced for an equal voltage rating.
Secondly, lower leakage currents happen for SiC and GaN, as electron-hole pairs are generated much slower. This reduces leakage current losses in off-state when compared to Si given a fixed temperature. Also, higher switching frequencies are enabled due to better electron saturation velocities and greater thermal conductivity. It influences the material temperature where for high-power applications, component inefficiencies will generate heat. Increasing the temperature of the material, and with that the electrical characteristics of the device change accordingly. A lower on-state resistance decreases conduction losses. For Si unipolar devices the on-resistance becomes unacceptably high for increasing levels of breakdown voltage, causing slower switching speed and increasing switching losses as the on-state injected carriers must be removed before it reaches the off-state [21] [22].
The on-resistance limit for a SiC device equals [22]:

$$R_{on} = 2.95 * 10^{-11} V_B^{2.28} \ \Omega\text{cm}^2 \tag{32}$$

Where V_B is the device breakdown voltage. For SiC application, under high-voltage conditions unipolar devices with extremely low on-resistances (see 32) can be realised. This ensures fast and low-loss switching characteristics. The carrier density of SiC is less than one-tenth of that of Si, due to its wide bandgap (SiC, bandgap: 3.2 eV). Taking the energy efficiency of the designed ship architecture into consideration implementing SiC semiconductors would reduce losses increasing system efficiency [21] [22].
But now to be decisive on the choice between SiC and GaN, again referring back to the list of material parameters mentioned above, regarding their bandgap there is little difference between 3.2 eV for SiC versus 3.4 eV for GaN. For the thermal conductivity, the differences are more significant. Gallium nitride has a thermal conductivity of 1.3 W/cmK, silicon 1.5 W/cmK and silicon carbide 5 W/cmK. So, silicon carbide is better at transferring thermal loads making it advantageous in high-power applications where device heating becomes a problem. Therefore applying silicon carbide FETs in the dc/dc

converter between the dc bus and inverter and for the inverter itself is advantageous. The last parameter is on the breakdown fields typically measure in MV/cm. For gallium nitride, the breakdown field equals 3.3 MV/cm which is close to silicon carbide having a breakdown field of 3.5 MV/cm. Silicon itself has a breakdown field of 0.3 MV/cm, differentiating from SiC and GaN by the factor of 10 mentioned above. [23].
Conclusively both silicon carbide and gallium nitride are advantageous over plain silicon. Based on this, for the solar-powered pleasure yacht, implementing SiC FETs will up system efficiency.

III. Improvement(s)

Now, as the system is complete and fully functional a further look into efficiency will be next.
One way to increase this is by implementing ”soft switching”. All switching devices/power transistors used are now ”hard switched”. A FET's switching loss is approximated by [24]:

$$P_{loss} = \frac{1}{2} V_{DS} I_D t_{on} f_s \tag{33}$$

As the switching devices operate at relatively high frequencies they cause high switching losses and EMI. As f_s becomes larger the more the working of the system suffers from high dv/dt and di/dt. Besides, the time for the switch to turn on will always be of finite value. During turn-on, the full input signal is across the switching device as it changes state. During this period the voltage drops and the current increases until it reaches its steady state (see Fig. 26). This means that, as now both voltage over and current through the device are present, the power transistor dissipates power. The same process happens at device turn-off. Soft switching improves this, lowering the dissipated power, by letting the turn on and off process occur at nearly zero voltage (ZVS) or current (ZCS).

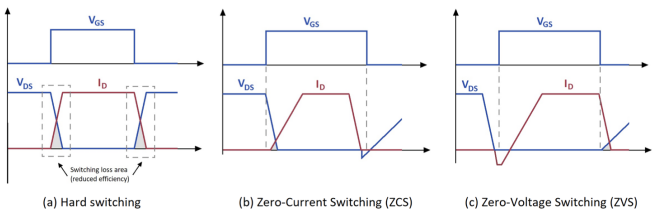

Fig. 26. Operating waveforms for conventional hard switching (a) and soft switching ZCS (b) and ZVS (c) of power transistor [25].

In converters containing MOSFETs and diodes, such as the implemented DAB, ZVS reduces switching losses caused by the power transistor output capacitances. ZCS, on the other hand, can mitigate the switching losses caused by current tailing present in IGBTs and stray inductances. Often, when diode recovered charge and semiconductor output capacitances are the dominant loss, ZVS is preferred [26].
Additionally, ZVS reduces the EMI associated with internal parasitic capacitances. High-frequency ringing and current spikes occur from the rapid charging and discharging (fast changing dV/dt) of the snubber capacitances [26] according to:

$$i_c = C \frac{dV}{dt} \tag{34}$$

A. Snubber Components

When referring back to Fig. 18, in between intervals one and two, there exists a small dead time. In this so-called dead time, the energy stored in the leakage inductor discharges the output capacitances of the MOSFETs, keeping them at or near zero volts before reaching their turn-on state again. This phenomenon makes ZVS-like behaviour possible for all of the lagging bridge switches (Q5-8) and some of the switches of the leading bridge (Q1-4) due to the lagging current. This technique is primarily used for protection, transferring the switching losses from the switching device to the snubber resistance. This does not influence the overall efficiency with sufficient margin but does help in thermal management as the semi-conductor devices have less heat to dissipate now. This is dependent upon the inductive energy [17]:

$$E_L = \frac{1}{2} L I_l^2 \tag{35}$$

As this needs to be sufficient to both charge and discharge the output capacitances of the MOSFETs according to [17]:

$$E_C = \frac{1}{2} C V_C^2 \tag{36}$$

When transition happens from interval one to two for the primary side switches, Q1 and Q4 remain closed and conducting, whereas for the secondary TF side, Q6 and Q7 open and Q5 and Q8 close and start conducting. Initially, when Q6 and Q7 are conducting the voltage across them equals zero (ideally) with Q5 and Q8 blocking blocking the full secondary side voltage. During dead time in between interval one and two, when all switches are in off-state, the energy stored in the inductor ensures a circulating current discharging C_{Q5} and C_{Q8} and charges C_{Q6} and C_{Q7} to V_D [17].
Once charged and discharged within one cycle, a current flow is needed again, realized by the FETs body diode through D_{Q5} and D_{Q8} clamping the voltage across the corresponding FETs to zero. In the following interval Q5 and Q8 are turned on at/near zero voltage, reducing the turn on losses [17]. This process is depicted in Fig. 27 based on [17], where the current paths are given in red.

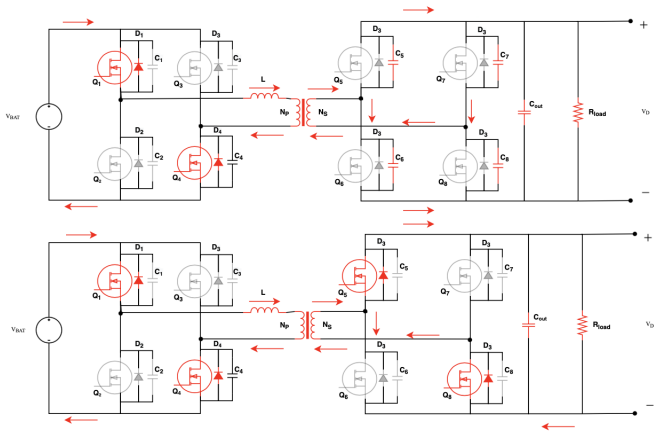

Fig. 27. ZVS transition on secondary TF side with current paths given in red.

Achieving this across the primary side switches, happens during the transition from interval 2 to 3 (see Fig. 28 based on [17]). The secondary TF side switches Q5 and Q8 continue conduction, whereas on the primary side switches Q1 and Q4 stop conducting and Q2 and Q3 start conducting. Here the same story holds true, as initially the voltage across Q1 and Q4 is zero when conducting with transistors Q2 and Q3 blocking the entire secondary side voltage. During the small dead when primary side switches do not conduct, the inductor stored energy again circulates current. This discharges C_{Q2} and C_{Q3} to zero and charges C_{Q1} and C_{Q4} to V_{bat} [17]. Once charged and discharged within one cycle, a current flow is needed again realized by the FETs body diode through D_{Q2} and D_{Q3} clamping the voltage across the corresponding FETs to zero. In the following interval Q2 and Q3 are turned on at/near zero voltage, reducing the turn on losses [17].

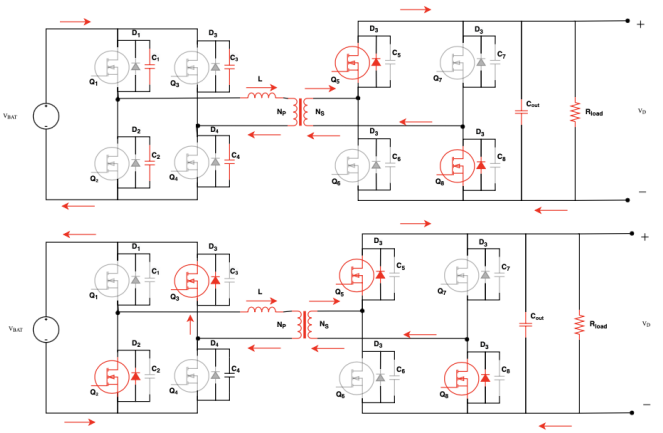

Fig. 28. ZVS transition on primary TF side with current paths given in red.

Now, each leg having two identical, internal snubber capacitances in parallel, with one being charged and the other being discharged the effective capacitance is 2C. Now the snubber capacitance and present inductance form a filter which resonates, with resonance frequency (f_r) which should be much higher than the FETs f_s. f_r is given as [27]:

$$f_r = \frac{1}{2\pi\sqrt{LC}} \tag{37}$$

Besides that to achieve the ZVS-like behaviour the energy stored in the inductor given by (35) should be sufficient to be able to charge and discharge the snubber and output filter capacitance. Therefore, the following relation holds true [27]:

$$\frac{1}{2}LI_L^2 = 2CV_{bat}V_D \tag{38}$$

This can be rewritten into an expression for the minimal inductor current [27]:

$$I_L = 2\sqrt{\frac{CV_{bat}V_D}{L}} \tag{39}$$

The duty ratio will not remain at 50%, as we introduced the concept of dead time to achieve ZVS. For boost mode ($V_{in} < V_{out} = V_{bat} < V_D$), the duty ratio is for ZVS is given by [27]:

$$d \geq 0.5 - \frac{1}{2V_D} + \frac{4}{T_s}\sqrt{\frac{V_{bat}LC}{V_D}} \tag{40}$$

B. Full Bridge LLC SRC

To achieve ZVS for all and/or part of the switching devices, as mentioned before, the inductor current should be such that it is sufficiently high to be able to fully charge and discharge the resonant capacitance. Analyzing the waveforms given in Fig. 18, the ZVS conditions can be specified for both full bridges by looking at the voltage conversion (M) and phase shift (PS) ratio. The ZVS boundaries are given in Fig. 29.

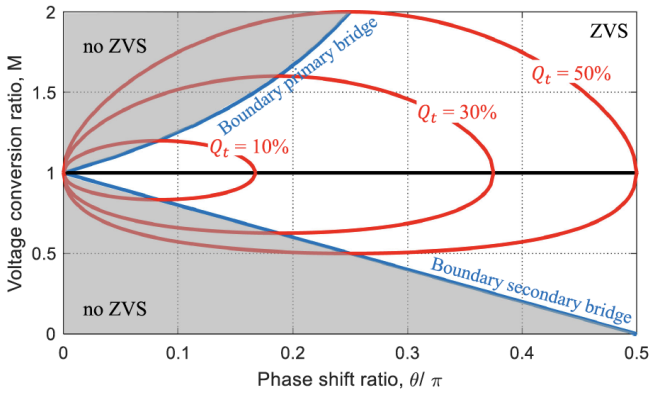

Fig. 29. ZVS boundaries for both primary and secondary full bridge of DAB [28].

For a voltage conversion ratio of 1, ideally, ZVS can be achieved over the full operating range. In case M differs, the phase shift must be sufficiently large to provide the required amount of energy to achieve ZVS. For small values of PS, meaning a low resistive load/high output power condition the ZVS range is limited. So, the converter should be designed such that it operates at maximum PS allowing higher currents. The trade-off here is that a greater PS between the voltage and current applied to one side of the TF results in higher reactive circulating currents increasing conduction losses [28].

ZVS is achieved by introducing a resonant circuit, consisting of a combination of L and C elements. Many topologies are used nowadays all having their advantages and disadvantages regarding their desired application. They vary in operating region, circulating energy, efficiency, light load voltage regulation, etc. Taking these parameters into consideration chosen is to use an LLC resonant tank due to its simplicity, wide ZVS operating region, the capability of light load voltage regulation, and high voltage gain possibilities [29].
A wide operation range is needed as the output voltage of the battery varies according to the state of charge, being dependent on the attached load and generated energy by the PV array. And so the converter needs to work for a wide input region, as stated in Sec. II-C2, with a regulated output dc bus voltage. On top of that, a significant voltage gain is needed between the battery and the dc bus. Many resonant tank topologies are not able to deliver such gains due to large circulating currents. For an LLC resonant converter the gain is given by [30]:

$$V_o = V_d = x * y * z * V_{in} = x * y * z * V_{bat} \tag{41}$$

with 'x' being the bridge switching gain equalling 0.5 for a half bridge implementation and 1.0 for full bridge, 'y' the resonant tank gain and 'z' the gain obtained from the turn ratio in the TF [30].
The LLC resonant tank gain can be derived by looking at the equivalent resonant circuit given in Fig. 30 based on [30].

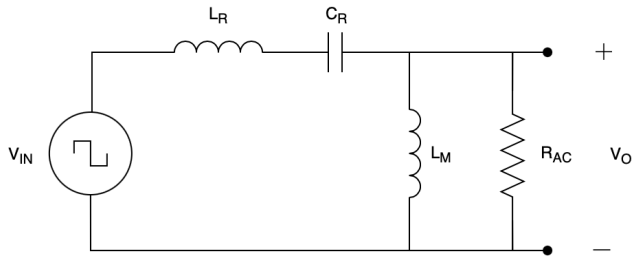

Fig. 30. LLC resonant tank equivalent circuit.

Here for the different impedances: $X_{L_R} = \omega L_R$, $X_{C_R} = \frac{1}{\omega C_R}$ and $X_{L_M} = \omega L_M$ using the First Harmonic Approximation (FHA) the transfer function is given by [30]:

$$G(Q, m, F_x) = \frac{|V_o|}{|V_{in}|} = \frac{F_x^2(m-1)}{\sqrt{(mF_x^2-1)^2 + F_x^2(F_x^2-1)^2(m-1)^2Q^2}} \tag{42}$$

where Q is the quality factor of the resonant circuit given as [30]:

$$Q = \frac{\sqrt{\frac{L_R}{C_R}}}{R_{ac}} \tag{43}$$

R_{ac} is the reflected load resistance [30]:

$$R_{ac} = \frac{8}{\pi^2} * (\frac{N_p}{N_s})^2 R_l \tag{44}$$

F_x is the normalized switching frequency, given as [30]:

$$F_x = \frac{f_s}{f_r} \tag{45}$$

Where f_s is the FETs switching frequency and f_r is the tank resonance frequency, given as [30]:

$$f_r = \frac{1}{2\pi\sqrt{L_R C_R}} \tag{46}$$

And lastly m is given as the ratio of total primary inductance to the resonance inductance (L_r) [30]:

$$m = \frac{L_R + L_m}{L_R} \tag{47}$$

Using these equations and implementing the code given in Sec. VII-G one can plot the tank gain curve (G) against F_x for different values of Q and m. Such a plot is given in Fig. 31 for randomly chosen values of Q and m.

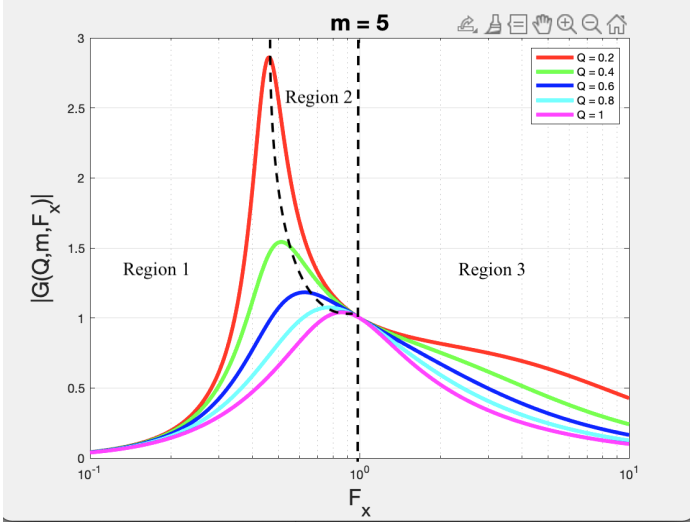

Fig. 31. Tank gain against normalized frequency for randomly chosen values of Q and m.

Fig. 31 is divided into three regions. Region one is on the left of the pure resistive curve (separation line between regions one and two). Here the converter works in its capacitive region where all primary bridge switches can work under ZCS condition. For region two the converter operates in boost mode, being the wanted region of operation. The input impedance is of inductive type with all primary bridge switches able to operate under ZVS and secondary bridge can achieve ZCS. For region three where $F_x > 1$ the operation equals that of a buck converter and operates in the inductive region [31].
The minimum and maximum voltage gain required from the resonant tank are dependent on the input voltage variation (V_{bat}). As the battery deals with a variety of charge and discharge conditions its voltage differs between 90 and 140 volts approximately (see Sec. II-C2). Therefore the G_{min} and G_{max} are given as:

$$G_{min} = \frac{V_{bat,nom}}{V_{bat,max}} = \frac{120}{140} = 0.86 \tag{48}$$

and

$$G_{max} = \frac{V_{bat,nom}}{V_{bat,min}} = \frac{120}{90} = 1.33 \tag{49}$$

The first step toward a final tank circuit design is now deciding on a Q and m value. For operation under heavy load conditions, a higher Q value is required, while lighter loads have lower Q values. So, the best way selecting Q is by setting a maximum value for Q operating under maximum load condition. The circuit is able to achieve higher boost gain but is less sensitive to frequency modulation and hence f_s has to significantly increase to reach the G_{min}, increasing switching losses [30]. Now, regarding the choice for the best value for m, a number of effects need to be mentioned. The lower m, the higher the possible boost gain that can be achieved. In addition, there is a more narrow range for FM, meaning less strict control is required. On the other hand, low values for m (for the same Q) goes hand in hand with smaller inductance values. This leads to greater ripple currents, increased circulating energies and conduction losses [30]. Q and m were selected at 0.4 and 3.1 respectively. The gain curve for these specific values is given in Fig. 32.

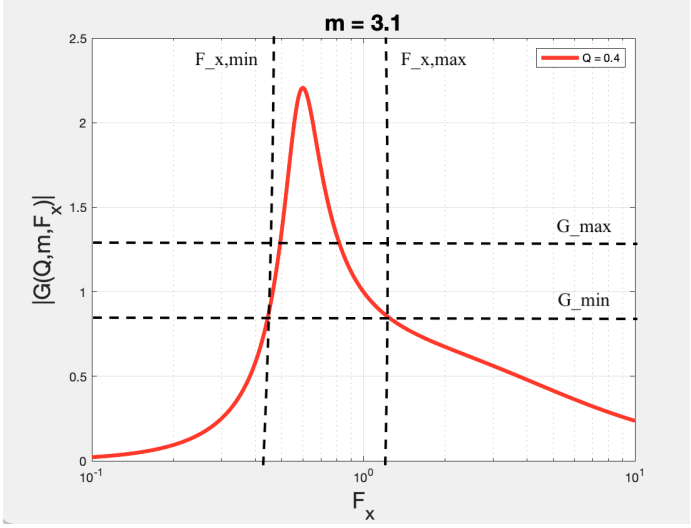

Fig. 32. Tank gain against normalized frequency for m = 3.1 and Q = 0.4.

The resonance frequency is set at 125 kHz, and so from Fig. 32 the FETs minimal f_s can be derived:

$$f_{s,min} = F_{x,min} * f_r = 0.34 * 125kHz = 42.5kHz \tag{50}$$

Now, as a check-up, as the power is derated at possible lower input voltages the maximum value for Q is needed at the minimum input voltage according to:

$$Q_{max@v_{min}} = Q_{max} * \frac{V_{in,min}}{V_{in,max}} = 0.4 * \frac{90}{140} = 0.257 \tag{51}$$

Substituting this in (42) the maximum gain for minimal f_s is derived:

$$\begin{aligned} G(Q_{max@V_{in}}, m, F_{x,min}) &= G(0.257, 3.1, 0.34) \\ &= 1.47 > G_{max} = 1.33 \end{aligned} \tag{52}$$

Now using (43 - 47) the component values can be derived. All parameters are given in table II.

TABLE II
RESONANT TANK COMPONENT VALUES.

Parameter	Value	Description
L_R	$0.396\mu H$	Resonance Inductance
L_M	$0.832\mu H$	Magnetizing Inductance
C_R	$4.09\mu F$	Resonance Capacitance
F_r	125 kHz	Resonance Frequency
R_{ac}	0.37Ω	Reflected load resistance

Implementing this in MATLAB Simulink was done with a change in topology, dropping the bidirectional power flow feature. The secondary full bridge was replaced with a diode rectifier due to increasing complexity in control using SPSM and limited ZVS range due to the required gain, which can be seen in Fig. 29. The implemented circuitry is given in Fig. 33.

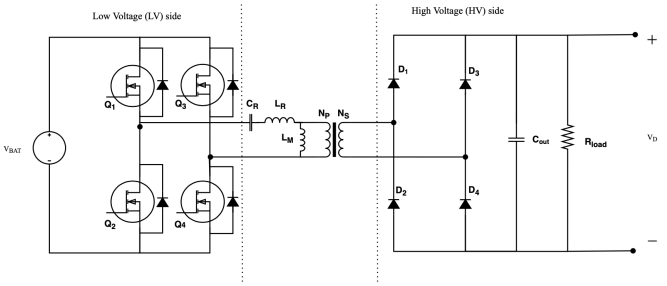

Fig. 33. Full bridge LLC series resonant converter circuitry.

Controlling the dc bus voltage now, as no secondary full bridge is present, is done by controlling the switching frequency of the primary full bridge (FSM) for the circuit implementation in MATLAB Simulink see Sec. VII-H. As the operating principle is more or less the same as explained in Fig. 17 it will only be explained briefly. The working operation is divided into 5 consecutive modes given in Fig. 34.

1) Mode 1: During the first period switches, Q2 and Q3 conduct and power is delivered from the battery to the attached load. The primary side inverter current gradually decays through diodes D1 and D4 [32].

2) Mode 2: Here the magnetizing current appears on the primary TF side. The secondary TF side current equals zero at ZCS and so D1 and D4 turn off [32].

3) Mode 3: For the third period, switches Q1 and Q4 conduct with Q2 and Q3 turning off under ZVS condition. On the secondary side, the current flows through diodes D2 and D3 [32].

4) Mode 4: In the fourth mode, the primary side current reverses and so the secondary side current deliberately rises from zero. Power gets transferred from the battery to the load through the use of the resonant tank circuit [32].

5) Mode 5: In the last of the five modes power is transferred from source to load by means of the resonant tank. The current polarity inverses, introducing the next half cycle following the same principle as described in mode 1 [32].

To control the stable output voltage a Discrete PI controller, with gains $K_p = 10000$ and $K_i = 1$, is used in a negative

feedback loop outputting the desired f_s. Its output is limited at a peak f_s of 153 kHz, according to:

$$f_{s,max} = F_{x,max} * f_r = 1.225 * 125 * 10^3 = 153\ kHz \quad (53)$$

The output of the PI controller is used as input to a sinusoidal function, outputting *sin(u)* with u being the input. The *asin* gives an argument between –1 and 1, and is equal to the angle in radians, effectively reshaping the sinusoidal input to a triangular output with equal frequency. The function takes the triangular input function and re-scales it between 0 and 1 after which a form of PWM is used to drive the FET gates (see Sec. VII-H). Fig. 34 shows the expected waveforms based on [33].

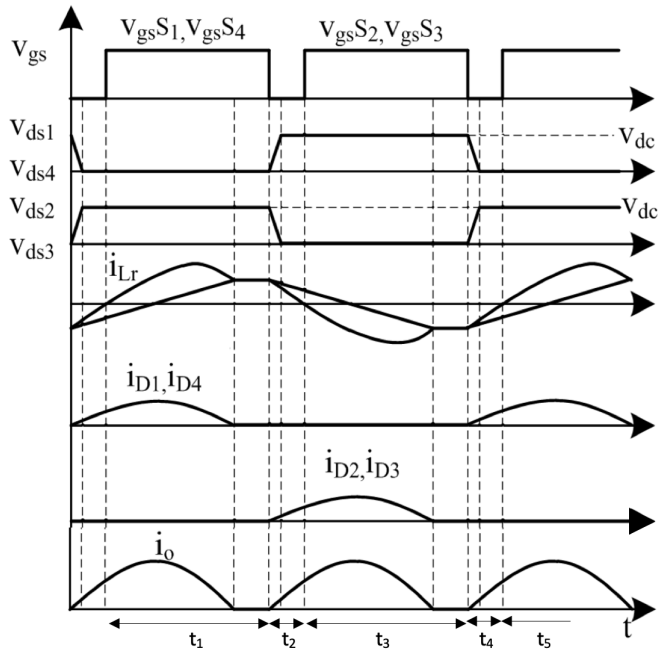

Fig. 34. Key waveforms for LLC resonant converter.

Using the values given in Table II and implementing the circuit in Simulink these waveforms can be verified to achieve a stable dc bus voltage value neglecting the dead time of the FETs. Fig. 44 in Sec. VII-I shows the output waveforms from MATLAB Simulink proving the correct operating of the circuitry. Fig. 35 shows V_{ds} and I_d present in Q4 (see Fig. 33).

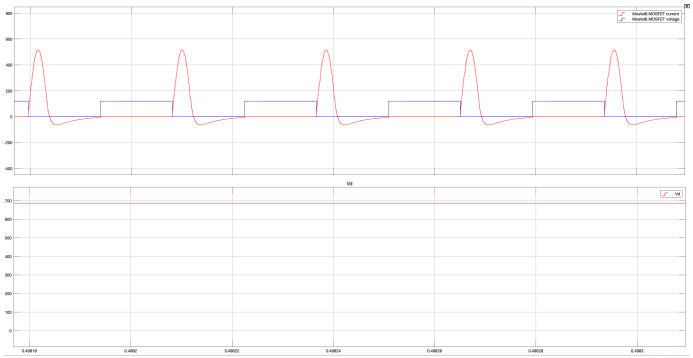

Fig. 35. Vds and Id (top) and dc bus voltage (bottom).

It can be seen that ZVS is successfully achieved at turn-on and a steady dc bus voltage is achieved. Now, attaching the rest of the system (see Sec. VII-J) leads to similar results as described in Sec. II-F achieving a fully operating system.
Taking a critical look at the DBDSRC, using two active full bridges would have been superior enabling features such as bidirectional operation, higher efficiencies due to higher internal losses in the passive rectifier, power regulation and dynamic load responses. Applying an active rectifier operated at a switching frequency for which the maximum tank gain is reached, the PI controller will take care of the output voltage regulation. By again controlling the phase shift between the two bridges the power transfer can be regulated by operating all switching devices at 50% duty cycle. This topology is attractive in literature due to the low number of components needed for the resonant network. Commonly, the DABSRC is frequency operated, adjusting the switching frequency of the FETs, however, a wide switching frequency range is needed to properly control the power transfer (see Fig. 32). This complicates both the control and the resonant tank filter design. A second control method is applying phase shift control, which requires a careful choice of both phase-shift and switching frequency. Commonly, in literature, these issues are treated with respect to output power, making the analysis design specific. Modelling and closed-loop control of the DABSRC is rather underdeveloped in literature.

IV. Load curve

As a consumer, one is interested in the power consumption of such a yacht over time. As the designed model still includes too many idealities, interchangeable products from the industry have been taken accordingly. All implemented products are given in Sec. VII-K with Table III including all power ratings for the corresponding devices and their expected on-time. The converter efficiencies were taken into account and regarding the asynchronous motor, a representative replacement was taken with an equal power rating.

TABLE III
ONBOARD DEVICES INCLUDING POWER CONSUMPTION AND ASSUMED ON-TIME [34] [35] [36] [37] [38] [39] [40] [41].

Device	Power (W)	Time
Refrigerator	10.9	00:00-23:00
TV	10	18:00 - 22:00
Radio	15	8:00 - 17:00
Lights (Inside)	25	22:00 - 23:00
Lights (Outside)	25	22:00 - 8:00
Bridge	36	00:00 - 23:00
Accessories	5	22:00 - 23:00
Kitchen	1500	25% 9:00, 25% 12:00, 50% 17:00

A situation is sketched for a sunny day in July having 2 passengers on board. Using the devices given in table III consuming energy for the given time periods, the following two graphs represent the power levels for the corresponding subsystems and battery SOC over a 24 hours time span. Regarding the generated energy by the PV array, it is assumed to have a sunny day with 5 full sun hours averaging the proceeds according to [42]. The total panel power yield is approximated by:

$$P_{delivered} = 5ncP_{wp}\eta = 5 * 3 * 0.85 * 225 * 0.98 = 2,8\ kWh \tag{54}$$

where n is the number of panels, c is a correction factor for the panels not having the ideal angle of irradiance, P_{wp} the panel peak power [11] and η the MPPT efficiency factor [43].

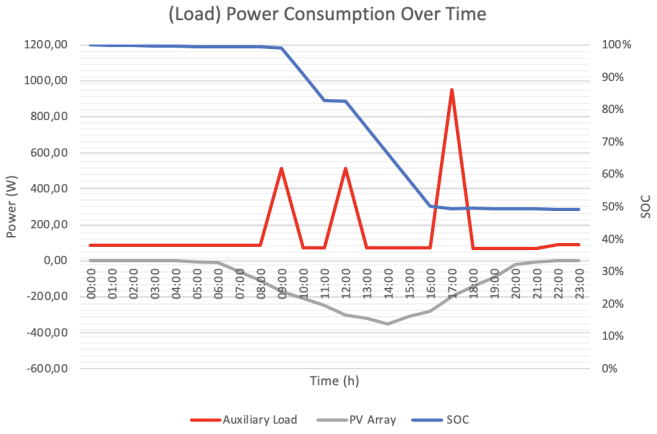

Fig. 36. Power consumption over time for auxiliary load, incoming PV and battery SOC.

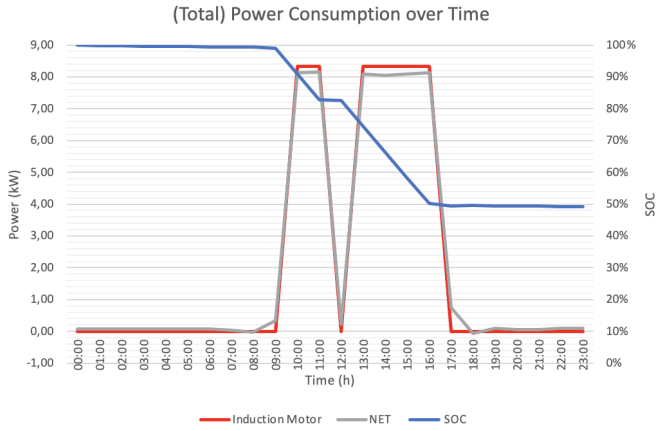

Fig. 37. Power consumption over time for induction motor, the netto power consumption and battery SOC.

From Fig. 36 and 37, the conclusion can be drawn that the designed system is able to operate for approximately 1,5-2 days without being dependent on shore power based on Sec. VII-L. Taking the average price of a kWh into consideration [44] Table VII displays the daily energy cost. In comparison, the daily fuel cost (E10) is given under the assumption of again 6 hours of sailing at half throttle for a 20 hp (15 kW) Honda outboard engine with a fuel consumption approximated at 3 litres/hour. With the current gas price [45] this sums up to a total exceeding the price of a fully electric powered yacht by (leaving the auxiliary load driven by fuel generator out of scope):

$$\text{Cost diff./24h} = €42,59 - €27,91 = €14,68 \tag{55}$$

V. Conclusion

The aim of this thesis was to design and simulate a dc architecture-based system for an all-electric pleasure yacht. As the maritime industry is in desperate need of electrification to be able to contribute to the goals set in the Paris agreement, big changes are needed to reduce emission levels. Four subsystems are designed to contribute to the basics of the dc architecture; asynchronous 15 kW 3-Φ induction motor with 86.6% energy efficiency, MPPT using a step-up converter with 90.5% energy efficiency, step down converter powering auxiliary loads with 89.6% average energy efficiency and an LV to HV dc bus bidirectional DAB converter with 91.6% energy efficiency. All models are successfully verified by simulations using MATLAB Simulink. An analysis is included on the MOSFET snubber circuit and its ZVS-like capabilities, followed by a worked-out Full Bridge series resonant converter achieving ZVS at transistor turn-on based on mathematically derived resonant tank components. A comparison is made between the use of MOSFETs versus IGBT regarding the preferred operating boundaries to substantiate the choice of transistor type regarding breakdown voltages, frequency application and on-resistance. Furthermore, it is concluded how the implementation of SiC FETs over Si can contribute to higher efficiency levels. From a consumer-based view, load curves are included by taking interchangeable products from industry, representing

the designed system estimating the off-grid performance for a 24-hour time span. Taking into account the fossil fuel-based alternative, it is concluded that a €14,68 economic surplus on a daily basis is reached using current energy and fuel prices. Consequently, an operationally successful DC architecture-based system was designed for medium-sized vessel applications. Due to time constraints, no further improvements could be realised, but regarding future work, there is still scope for further performance enhancement.

VI. Future Work

Although the designed system is operatable and reasonable for real industrial application, several improvements are proposed.

First, for the DAB being a high-power converter a number of modulation schemes/topologies exist. In order for the DAB converter to actively control its power flow, different modulation strategies exist of which Single Phase Shift was used. Existing alternatives are, for example, Triangular Modulation (TRM) and Extended Single Phase Shift (ESPS). Literature proposes that EPS control extends the soft-switching capabilities of the DAB and hence, higher power transfer is possible for light-load conditions. This further increases converter efficiency at light-loads operation. This would also allow bidirectional power flow again, which would not be of interest for a purely motor-powered yacht but for sailing this could be an interesting feature.

The induction motor has a high start-up current no back EMF is present in the armature circuit for start-up conditions. To solve for this a soft starter is proposed, which protects AC motors from sudden power influxes. It limits the inrush current present during start-up and gradually increases until steady state condition [46].

For the battery voltage, 120V was chosen taking all converter gain ratios into consideration. In general, it holds true that higher voltage systems are more efficient as it experiences less resistive losses for equal power demand. In the EV industry battery packages of 400-800V are no exception. Therefore, it may be implemented for pleasure yachts as well.

For the closed-loop control strategy PI(D) controllers were used for their robust control in a wide range of operating conditions and functional simplicity. The tuning was done manually. To properly derive the optimal system gains one needs to come up with a representative mathematical model to derive the optimal gains.

Furthermore, for powering the auxiliary load a buck converter is required stepping down the dc battery voltage. The current step-down factor of 10 already introduces high currents for high power demand situations. When stepping up the battery voltage even further, as proposed, this becomes critical. Therefore, an isolated converter is proposed to provide galvanic isolation.

Lastly, to reach the goals set in the Paris Agreement the maritime industry as a whole is in strict need of electrification. The proposed system is applicable to medium-sized pleasure yachts and medium-high power applications. The real emission is not in the private sector but in the industry. Scaling this up, for an industry inland vessel or seagoing vessel very high power application is required (in the order of MW). Often diesel generators are implemented making it possible to swap this out for a battery pack. One example is currently in use [47], and fast charging is a challenge.

References

[1] "Vermindering van de emissies van de scheepvaartsector" european comission report," https://ec.europa.eu/clima/eu-action/transport-emissions/reducing-emissions-shipping-sector_nl, accessed: 19-6-2022.

[2] M. Mandasari. (2018, Diploma thesis for Master degree in Technology. Available at: Faculty of Engineering Science and Technology, Department of Electrical Engineering) Application of electric vehicle charging solutions on small maritime vessels.

[3] R. Electric. (1-6-2020. Available at: https://renown-electric.com/blog/ac-vs-dc-motors-whats-the-difference/) Ac vs. dc motors: What's the difference?

[4] M. K. Saini. (30-8-2021. Available at: https://www.tutorialspoint.com/speed-control-of-induction-motor) Speed control of induction motor.

[5] B. K. Bose, *Modern Power Electronics and AC Drives*. The University of Tennessee, Knoxville: Prentice Hall PTR, 2002.

[6] *Basic Understanding of Converter (Sinusoidal Pulse width Modulation and Three Phase Circuit)*. Indian Institute of Technology Delhi, July 2018. [Online]. Available: https://www.youtube.com/watch?v=UX2GuyPBQc4&t=2152s

[7] *Mechanical Dynamics, the Swing Equation, Units*. Iowa State University, College of Engineering. [Online]. Available: https://home.engineering.iastate.edu/~jdm/ee554/SwingEquation.pdf

[8] J. P. Torreglosa, E. González-Rivera, P. García-Triviño, and D. Vera, "Performance analysis of a hybrid electric ship by real-time verification," *Energies*, vol. 15, no. 6, 2022. [Online]. Available: https://www.mdpi.com/1996-1073/15/6/2116

[9] D. Aicha, M. Rezaoui, and A. Teta, "Comparative study of perturb-and-observe and incremental conductance mppt methods for pv system," in *Second International Conference on Electrical Engineering "ICEEB'18 "*, 12 2018.

[10] I. Hamdan, A. Maghraby, and O. Noureldeen, "Stability improvement and control of grid-connected photovoltaic system during faults using supercapacitor," *SN Applied Sciences*, vol. 1, 12 2019.

[11] Bosch. (Version 01/2012. Available at: https://www.solarchoice.net.au/wp-content/uploads/Bosch-Solar-Module-c-Si-M-60-Australia.pdf) Powerful performance – high stability. bosch solar module c-si m 60 eu30117.

[12] T. Simulator. (14-09-2020. Available at: https://www.youtube.com/watch?v=o9BOrAHH5E4) Demonstration of maximum power point tracking (mppt) using boost converter in matlab - method 1.

[13] D. Xu, L. Wang, and J. Yang, "Research on li-ion battery management system," in *2010 International Conference on Electrical and Control Engineering*, 2010, pp. 4106–4109.

[14] T. INSTRUMENTS. (08-2015. Available at: https://www.ti.com/lit/an/slva477b/slva477b.pdf?ts=1656514696917&ref_url=https%253A%252F%252Fwww.google.de%252F) Basic calculation of a buck converter's power stage.

[15] C. Zhao, S. Round, and J. Kolar, "Full-order averaging modelling of zero-voltage-switching phase-shift bidirectional dc-dc converters," *Power Electronics, IET*, vol. 3, pp. 400 – 410, 06 2010.

[16] F. Krismer, "Modeling and optimization of bidirectional dual active bridge dc-dc converter topologies," Ph.D. dissertation, ETH Zurich, 2010.

[17] T. INSTRUMENTS. (2022 Available at: https://www.ti.com/lit/ug/tidues0b/tidues0b.pdf?ts=1653550733146) Bidirectional, dual active bridge reference design for level 3 electric vehicle charging stations.

[18] C. Blake, C. Bull, and I. Rectifier, "Igbt or mosfet: Choose wisely," *EngineerIT*, vol. 2018, 06 2022.

[19] E. Products. (3-10-2011. Available at: https://www.electronicproducts.com/mosfet-vs-igbt/) Mosfet vs. igbt: What is the difference and which is the better transistor?

[20] Alan. (24-11-2021. Available at: https://www.utmel.com/blog/categories/transistors/mosfet-vs-igbt-characteris tics-structure-and-market-analysis) Mosfet vs. igbt: Characteristics, structure and market analysis.

[21] J. Wang, "A comparison between si and sic mosfets," *IOP Conference Series: Materials Science and Engineering*, vol. 729, p. 012005, 02 2020.

[22] T. KIMOTO, "High-voltage sic power devices for improved energy efficiency," *Proceedings of the Japan Academy, Series B*, vol. 98, pp. 161–189, 04 2022.

[23] E. Products. (22-01-2020. Available at: https://www.arrow.com/en/research-and-events/articles/silicon-carbide-and-gallium-nitride-compared) Silicon carbide (sic) vs. gallium nitride (gan).

[24] T. McRae. (15-6-2021 2018. Available at: https://www.youtube.com/watch?v=nXwhJuNmGY0) Lecture 8.9: The dab and soft switching.

[25] A. Zhaksylyk, "Implementation of a phase shifted full bridge dc-dc zvs converter with peak current mode control," Ph.D. dissertation, UNIVERSIDAD DE OVIEDO, 08 2019.

[26] R. W. E. . D. Maksimovic, *Fundamentals of Power Electronics*. Springer, 2020.

[27] R. T. Naayagi, A. J. Forsyth, and R. Shuttleworth, "Performance analysis of dab dc-dc converter under zero voltage switching," in *2011 1st International Conference on Electrical Energy Systems*, 2011, pp. 56–61.

[28] S. Saeed, J. Garcia, and R. Georgious, "Dual-active-bridge isolated dc–dc converter with variable inductor for wide load range operation," *IEEE Transactions on Power Electronics*, vol. 36, no. 7, pp. 8028–8043, 2021.

[29] M. Arazi, A. Payman, M. B. Camara, and B. Dakyo, "Bidirectional interface resonant converter for wide voltage range storage applications," *Sustainability*, vol. 14, no. 1, 2022. [Online]. Available: https://www.mdpi.com/2071-1050/14/1/377

[30] S. Abdel-Rahman, "Resonant llc converter: Operation and design," *AN 2012-09*, V1.0 September 2012. Available at: https://www.infineon.com/dgdl/Application_Note_Resonant+LLC+Converter+Operation+and+Design_Infineon.pdf?fileId=db3a30433a047ba0013a4a60e3be64a1.

[31] S. A. Mortazavizadeh, S. Palazzo, A. Amendola, E. Santis, D. Ruzza, G. Panariello, A. Sanseverino, F. Velardi, and G. Busatto, "High frequency, high efficiency, and high power density gan-based llc resonant converter: State-of-the-art and perspectives," *Applied Sciences*, vol. 11, p. 11350, 11 2021.

[32] K. P. Panda and S. Rout, "A cost-effective design and analysis of full bridge llc resonant converter," *International Journal of Energy and Power Engineering*, vol. 10, no. 8, pp. 1143 – 1150, 2016. [Online]. Available: https://publications.waset.org/vol/116

[33] Y. Shen, W. Zhao, Z. Chen, and C. Cai, "Full-bridge llc resonant converter with series-parallel connected transformers for electric vehicle on-board charger," *IEEE Access*, vol. 6, pp. 13 490–13 500, 2018.

[34] *Freeline 115 Elegance Marine Refrigerators*, Indel Webasto Marine, 1 2016, available at: https://www.jpcdirect.com/wp-content/uploads/Isothern-Freeline-115-Data-Sheet.pdf.

[35] *Samsung UE32T5300C*, Samsung, available at: https://www.coolblue.nl/product/878753/samsung-ue32t5300c.html#product-information.

[36] *Philips M2805 Internetradio*, Philips, available at: https://www.download.p4c.philips.com/files/t/tam2805_10/tam2805_10_dfu_nld.pdf.

[37] *SUZUKI MULTI-FUNCTION DISPLAY*, Suzuki, available at: https://www.download.p4c.philips.com/files/t/tam2805_10/tam2805_10_dfu_nld.pdf.

[38] *SILVERCREST SDK 2500 B1 dubbele kookplaat instructies*, Silvercrest, available at: https://nl.manuals.plus/silvercrest/sdk-2500-b1-dual-hotplate-manual#axzz7WSjTIOgc.

[39] *BlueSolar Charge Controllers MPPT 75/10, 75/15, 100/15, 100/20 & 100/20-48V*, Victron Energy, available at: https://www.victronenergy.nl/upload/documents/Datasheet-Blue-Solar-Charge-Controller-MPPT-75-10,-75-15,-100-15-&-MPPT-100-20-NL.pdf.

[40] *Orion DC-DC-omvormers 110V, geïsoleerd*, Victron Energy, available at: https://www.victronenergy.nl/upload/documents/Datasheet-Orion-110-12V-30A-and-110-24V-15A-Isolated-DC-DC-converters-NL.pdf.

[41] *E-Tech KATALOG / CATALOGUE 2019*, E-Tech, available at: https://clouds.nl/wp-content/uploads/2019/03/E-TECH-catalogue-2019-internet.pdf.

[42] V. Dekker. (29 July 2019) Door de extreme hitte lopen we massaal zonnestroom mis. [Online]. Available: https://www.trouw.nl/duurzaamheid-natuur/door-de-extreme-hitte-lopen-we-massaal-zonnestroom-mis~bb441550/?referrer=https%3A%2F%2Fwww.google.com%2F

[43] *BlueSolar Charge Controllers MPPT 75/10, 75/15, 100/15, 100/20 & 100/20-48V*, Victron Energy, available at: https://www.victronenergy.nl/upload/documents/Datasheet-Blue-Solar-Charge-Controller-MPPT-75-10,-75-15,-100-15-&-MPPT-100-20-NL.pdf.

[44] "Stroomprijs," https://www.overstappen.nl/energie/stroomprijs/, accessed: 06-2022.

[45] "Brandstofprijzen europa," https://www.anwb.nl/vakantie/reisvoorbereiding/brandstofprijzen-europa, accessed: 18-6-2022.

[46] J. Larabee, B. Pellegrino, and B. Flick, "Induction motor starting methods and issues," in *Record of Conference Papers Industry Applications Society 52nd Annual Petroleum and Chemical Industry Conference*, 2005, pp. 217–222.

[47] P. of Rotterdam. (06-09-2021. Available at: https://www.portofrotterdam.com/en/news-and-press-releases/first-emission-free-inland-shipping-vessel-on-energy-containers-in-service) First emission-free inland shipping vessel on energy containers in service.

VII. Appendix

A.

TABLE IV
ASYNCHRONOUS MOTOR PARAMETERS.

Parameter	Value	Description
RMS line voltage	400 V	-
Nominal Power	20 HP (15 kW)	-
Frequency	50 Hz	-
Max. Rotor speed	1460 RPM	-
R_s	0.2147Ω	Stator Resistance
R_r	0.2205Ω	Rotor Resistance
L_s	0.000991 H	Stator Inductance
L_r	0.000991 H	Rotor Inductance
M	0.06419 H	Mutual Inductance
J	$0.102kg * m^2$	Inertia
F	0.009541 N*m*s	Friction Factor
P	2	Pole Pairs

B.

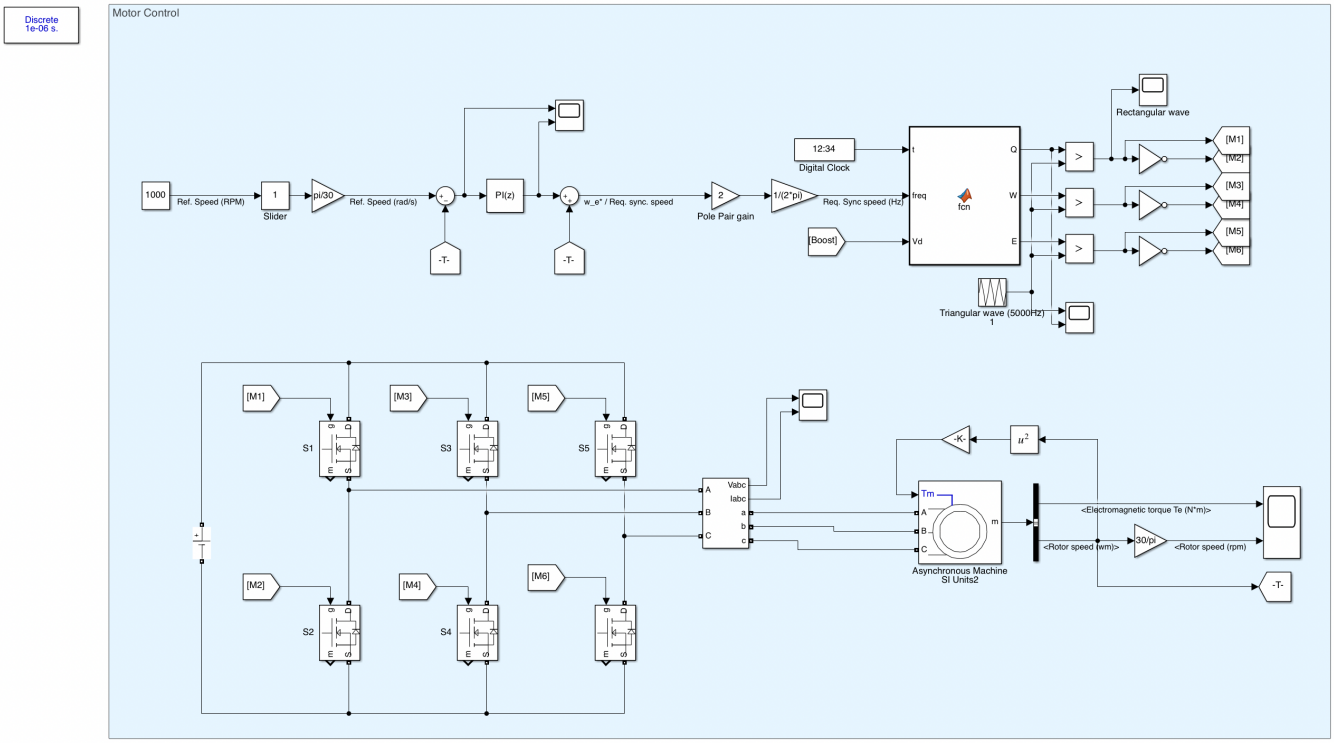

Fig. 38. MATLAB closed loop implementation of volt per hertz control of a variable frequency drive using PI control and sPWM.

C.

TABLE V
PV PANEL PARAMETERS [11].

Parameter	Value	Description
P_{max}	224.985 W	Maximum Power
N_{cell}	60	Cells per module
V_{oc}	36 V	Open Circuit Voltage
I_{sc}	8.7 A	Short-circuit current
V_{mp}	28.3 V	Voltage at maximum power point
I_{mp}	7.95 A	Current at maximum power point
-	-0.374 $\%/°C$	Temperature coefficient of V_{oc}
-	0.071 $\%/°C$	Temperature coefficient of I_{sc}

D.

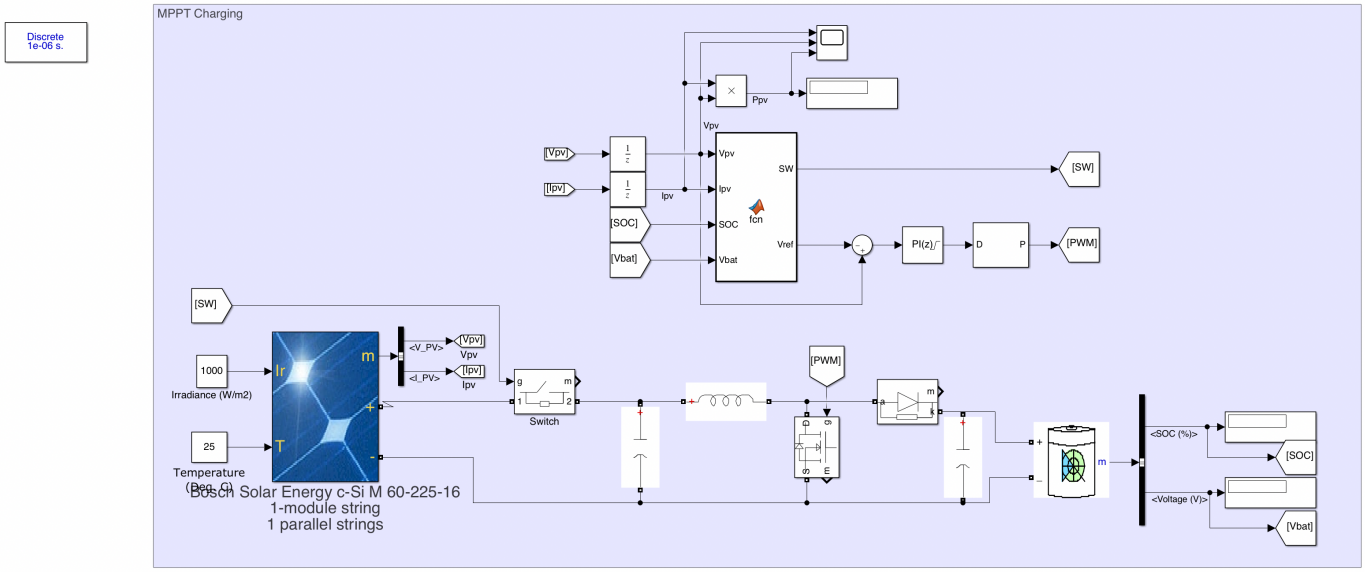

Fig. 39. P&O based closed loop MPPT control charging a battery using PI control and PWM.

E.

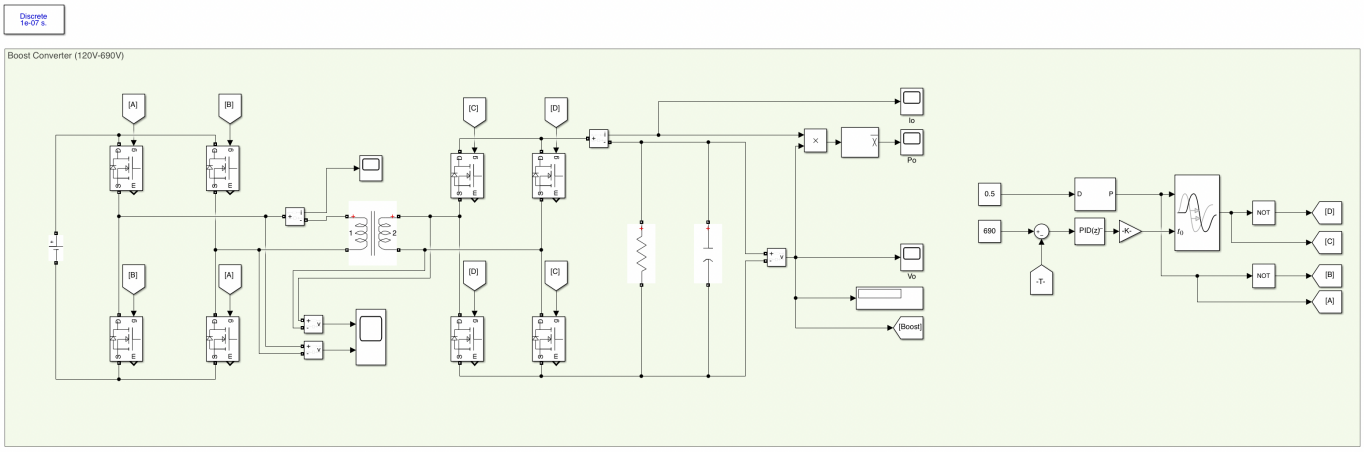

Fig. 40. DAB DC/DC converter implementation in MATLAB Simulink using closed loop control.

F.

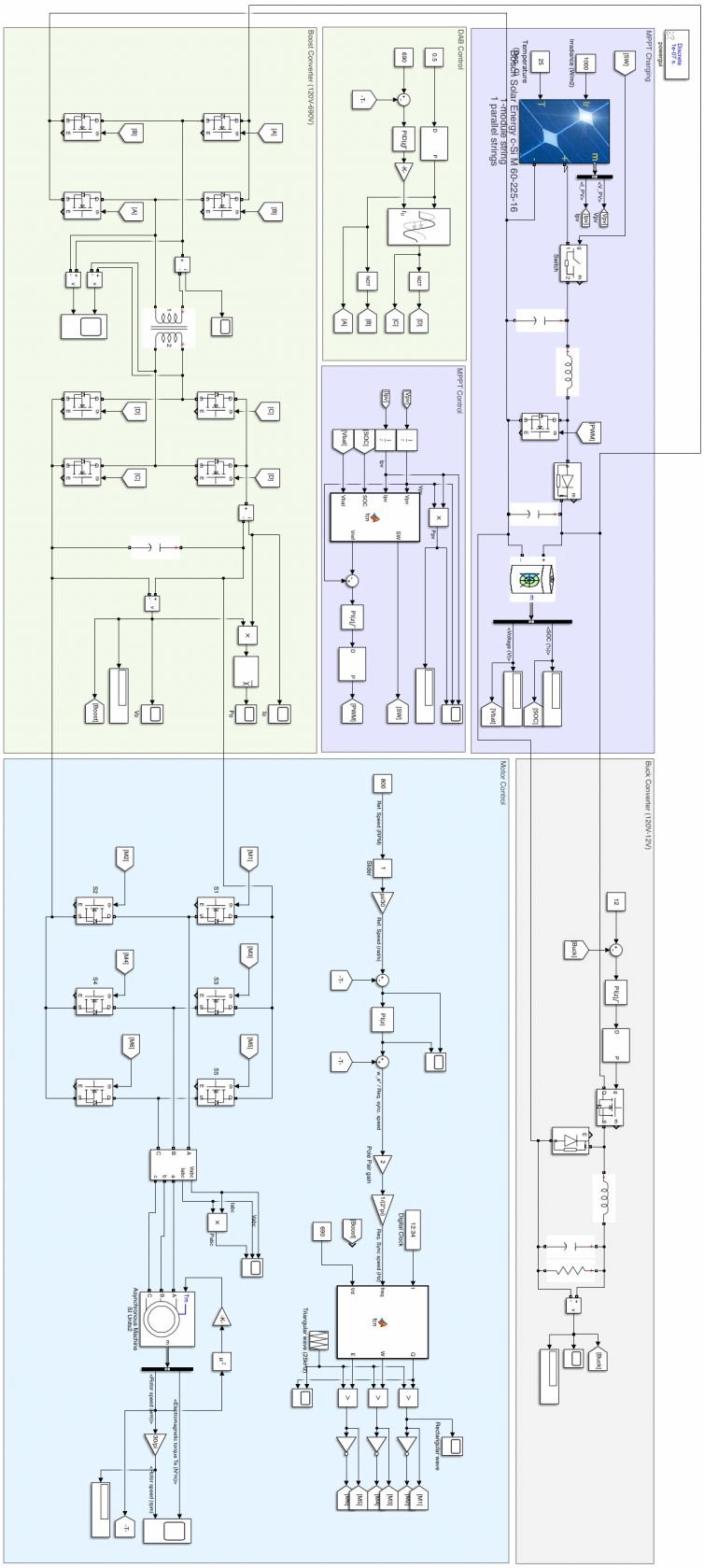

Fig. 41. Full system overview implemented in MATLAB Simulink.

G.

untitled.m | untitled2.m

```
clc;
clear all;
close all;

m = [1 2 3 4 5];
Fx = logspace(-1,1,1000);
colors = ['r' 'g' 'b' 'c' 'm'];
Q = [0.2 0.4 0.6 0.8 1.0];
for y = 1:5
    figure
    for i = 1:5
        Gain = (((Fx.^2)*(m(y)-1))./(((m(y)*(Fx.^2)-1).^2 + ((Fx.^2).*((Fx.^2)-1).^2).*((m(y)-1).^2)*(Q(i)^2)).^0.5));
        semilogx(Fx,Gain,'color', colors(i),'LineWidth',3)
        hold on
    end
    legend('Q = 0.2', 'Q = 0.4', 'Q = 0.6', 'Q = 0.8', 'Q = 1')
    title(['m = ', num2str(m(y))],'FontSize', 18)

xlabel('F_x','FontSize',18)
ylabel('|G(Q,m,F_x)|','FontSize',18)
grid on

end
```

Fig. 42. MATLAB code implemented to plot tank gain.

H.

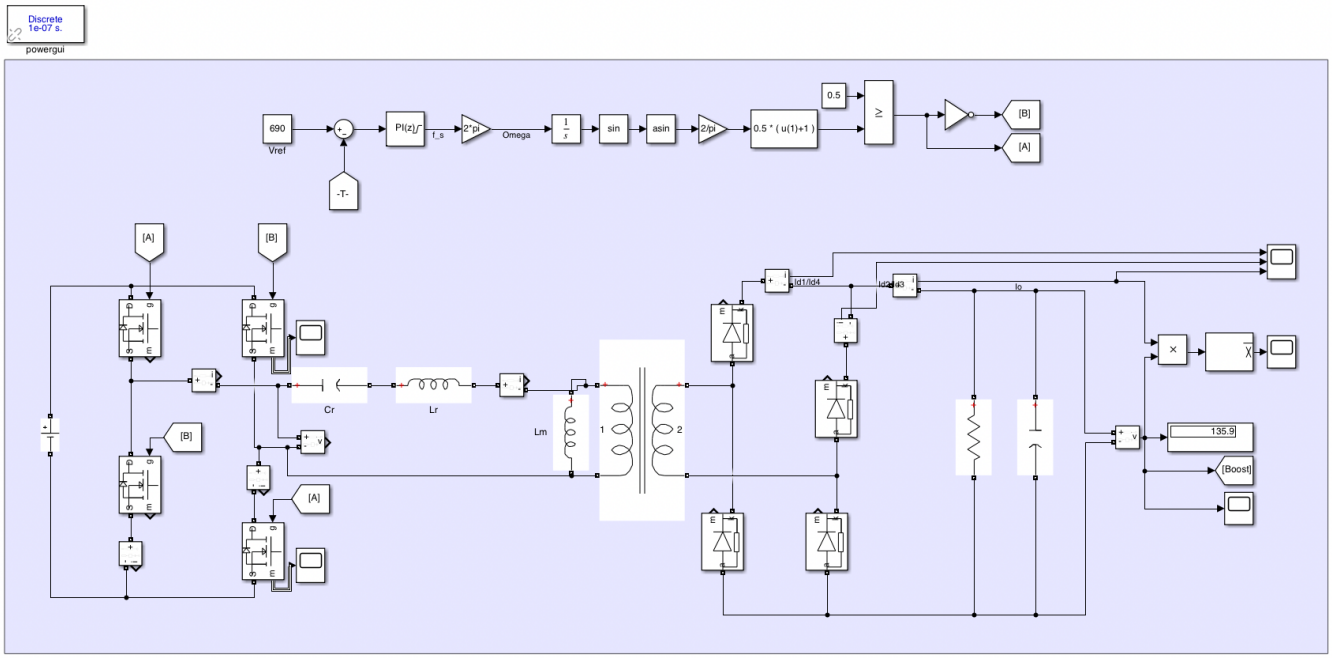

Fig. 43. LLC full bridge series resonant converter MATLAB Simulink circuitry.

I.

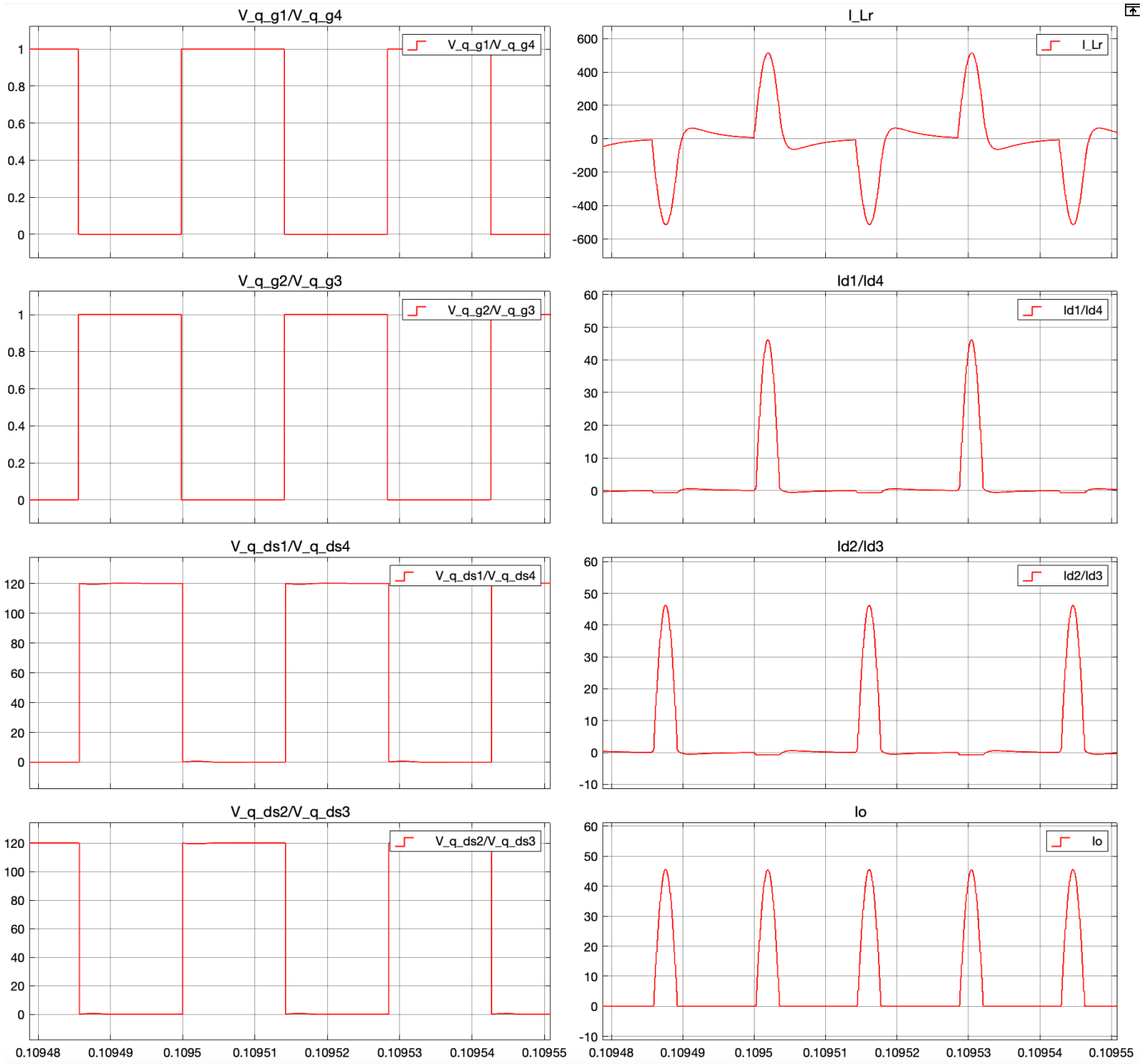

Fig. 44. Key waveforms for LLC resonant converter obtained from Simulink model.

J.

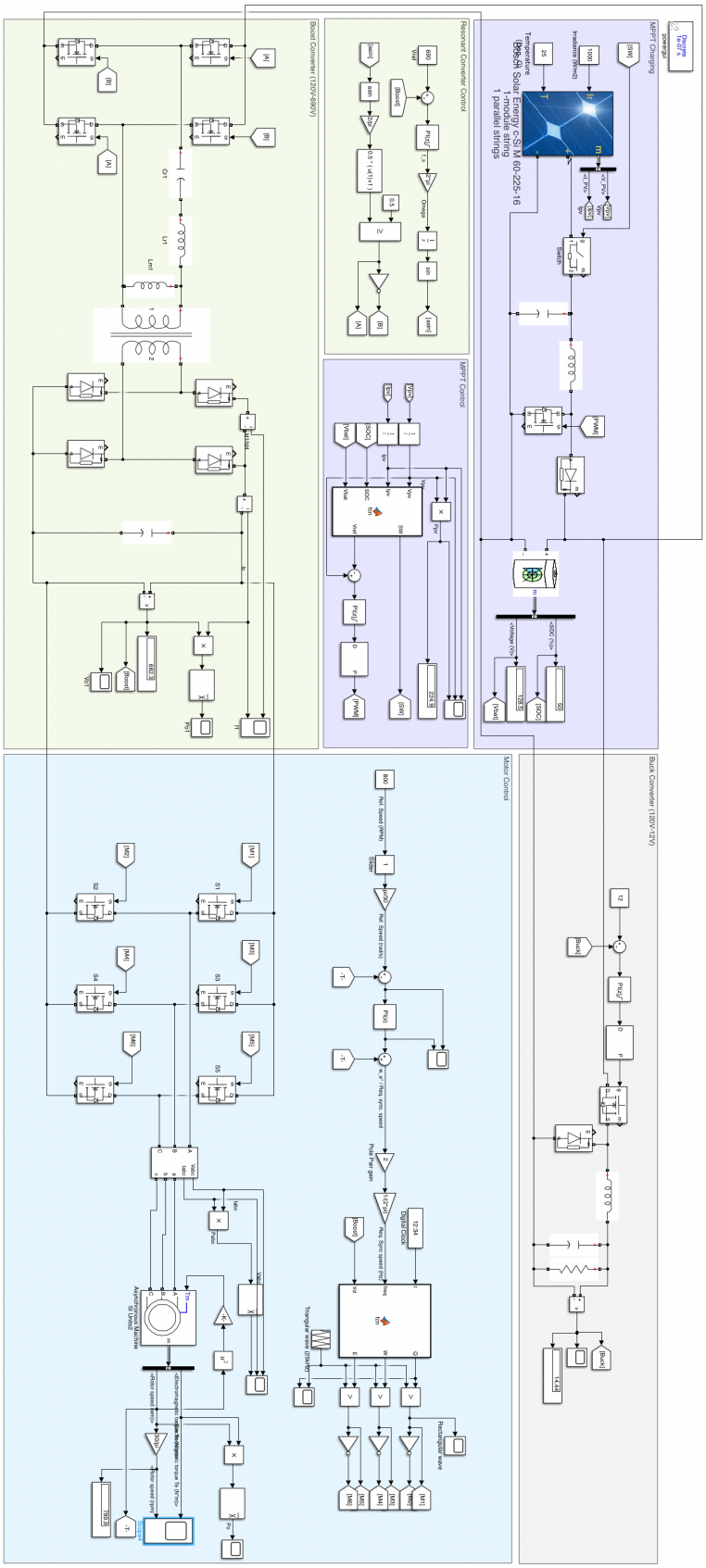

Fig. 45. Full system overview implemented in MATLAB Simulink with ZVS series resonant converter.

K.

TABLE VI
LIST OF IMPLEMENTED PRODUCTS FOR LOAD CURVE INCLUDING CONVERTER EFFICIENCY LEVELS [34] [35] [36] [37] [38] [39] [40] [41].

Device	Type	Efficiency
Refrigerator	Freeline 115 Elegance Marine Refrigerators	-
TV	Samsung UE32T5300C	-
Radio	Philips Internetradio M2805	-
Bridge	Suzuki SMD16	-
Kitchen	SILVERCREST® Dubbele inductiekookplaat	-
MPPT Converter	BlueSolar Charge Controllers MPPT 75/10 Victron Energy	98%
Isolated DC/DC Converter	Victron Energy Orion 110	85%
3-Φ Induction motor	E-Tech 15 POD	90%

L.

TABLE VII
ENERGY CONSUMPTION OF PROPOSED SYSTEM OVER A 24H BASIS [44] [45].

PV Powered Boat Power Curve + Cost Analysis					
Parameters	Value	Date			
Price/Litre (E10)	€ 2,366	17-06-2022			
Price/kWh	€ 0,549	16-06-2022			
Battery Capacity (kWh)	100				

Hours		Induction Motor (W)	Auxiliary Load (W)	PV Array (W)	NET	SOC
00:00		0,00	84,59	0	84,59	0,999
01:00		0,00	84,59	0	84,59	0,998
02:00		0,00	84,59	0	84,59	0,997
03:00		0,00	84,59	0	84,59	0,997
04:00		0,00	84,59	0	84,59	0,996
05:00		0,00	84,59	-5	79,59	0,995
06:00		0,00	84,59	-10	74,59	0,994
07:00		0,00	84,59	-60	24,59	0,994
08:00		0,00	84,59	-110	-25,41	0,994
09:00		0,00	514,00	-170	344,00	0,991
10:00		8333,33	72,82	-210	8126,16	0,910
11:00		8333,33	72,82	-250	8156,16	0,828
12:00		0,00	514,00	-300	214,00	0,826
13:00		8333,33	72,82	-320	8086,16	0,745
14:00		8333,33	72,82	-350	8056,16	0,664
15:00		8333,33	72,82	-310	8096,16	0,583
16:00		8333,33	72,82	-280	8126,16	0,502
17:00		0,00	949,29	-200	749,29	0,495
18:00		0,00	66,94	-140	-73,06	0,495
19:00		0,00	66,94	-90	90,00	0,495
20:00		0,00	66,94	-20	46,94	0,494
21:00		0,00	66,94	-5	61,94	0,493
22:00		0,00	90,47	0	90,47	0,493
23:00		0,00	90,47	0	90,47	0,492
Total		**50000**	**3624,24**	**-2830,00**	**50837,29**	

Cost price/day (Electric)	€ 27,91
Cost price/day (Fuel)	€ 42,59